

## RESEARCH ARTICLE

10.1002/2016GC006579

## REEBOX PRO: A forward model simulating melting of thermally and lithologically variable upwelling mantle

Eric L. Brown<sup>1</sup> and Charles E. Lesher<sup>1,2</sup><sup>1</sup>Department of Geoscience, Aarhus University, Aarhus, Denmark, <sup>2</sup>Department of Earth and Planetary Sciences, University of California, Davis, California, USA

## Key Points:

- REEBOX PRO is an executable program for PC and Mac simulating adiabatic decompression melting of lherzolite and pyroxenite
- The model outputs the mean trace element and isotopic composition of the bulk crust and all model melt compositions
- The model is benchmarked against existing models and is flexible enough for a wide range of melt pooling scenarios

## Supporting Information:

- Supporting Information S1
- Data Set S1
- Data Set S2
- Data Set S3

## Correspondence to:

E. L. Brown,  
ericlb@geo.au.dk

## Citation:

Brown, E. L., and C. E. Lesher (2016), REEBOX PRO: A forward model simulating melting of thermally and lithologically variable upwelling mantle, *Geochem. Geophys. Geosyst.*, 17, 3929–3968, doi:10.1002/2016GC006579.

Received 5 AUG 2016

Accepted 20 SEP 2016

Accepted article online 26 SEP 2016

Published online 20 OCT 2016

© 2016. The Authors.

This is an open access article under the terms of the Creative Commons Attribution-NonCommercial-NoDerivs License, which permits use and distribution in any medium, provided the original work is properly cited, the use is non-commercial and no modifications or adaptations are made.

**Abstract** The compositions and volumes of basalts erupted in divergent margin environments provide a record of the thermal, chemical, and dynamical state of their mantle source regions. To relate basalt compositions and volumes to the underlying thermochemical and dynamical state of their mantle source regions, we have developed REEBOX PRO, a compiled stand-alone application that simulates adiabatic decompression melting of passively or actively upwelling mantle containing up to five distinct lithologies. The model calculates melt compositions using thermodynamic and experimental constraints on the melting behaviors and mineral-melt partitioning behavior of homogeneous and lithologically heterogeneous mantle sources containing anhydrous peridotite, hydrous peridotite, harzburgite, and/or silica-saturated/-undersaturated pyroxenite. Key model outputs include the mean composition and crustal thickness for the bulk basaltic crust, calculated for passive and active upwelling scenarios. Here, we present the mathematical formulations underlying the model and benchmark it against existing hydrous melting models and models for mid-ocean ridge basalt formation. We show that the hydrous and anhydrous peridotite melting models incorporated in REEBOX PRO capture the essential differences in basalt composition and volume demonstrated by previous models, and constrain the ambient mantle beneath the global spreading ridge system to be between 1319 and 1366°C, depending on the relative fertility and/or water content of the mid-ocean ridge mantle source. We also show how model outputs may be manipulated outside of the modeling program to calculate nontraditional melt mixing scenarios. These examples highlight the flexibility of REEBOX PRO for simulating melt generation within a range of geodynamical contexts.

## 1. Introduction

Basaltic magmatism occurring at divergent margin, convergent margin, and intraplate settings is a fundamental process in the ongoing thermal, chemical, and physical evolution of our planet. Primitive basalt is most commonly formed by adiabatic decompression melting of mantle and represents an aggregate of melts derived over a range of pressures and temperatures [e.g., Klein and Langmuir, 1987; Johnson et al., 1990; Langmuir et al., 1992; Kelemen et al., 1995, 1997; Stracke et al., 1999, 2003a]. The composition and volume of basalts produced by decompression melting are functions of mantle temperature, composition, and mineralogy, as well as the thermodynamics of melting, upwelling rate, and dynamics of melt extraction [e.g., Spiegelman and McKenzie, 1987; Langmuir et al., 1992; Hirschmann and Stolper, 1996; Phipps Morgan, 2001; Asimow et al., 2001; Klein, 2003; Stracke et al., 2003a, 2003b; Ito and Mahoney, 2005; Stracke et al., 2006; Stracke and Bourdon, 2009]. For these reasons, the composition and volume of basaltic liquids derived from the mantle provide (in combination) quantitative constraints on the thermochemical and dynamical state of the mantle.

Fundamental to this endeavor has been the development and application of mantle melting models to basalt petrogenesis. For example, Langmuir and coworkers [Klein and Langmuir, 1987; Langmuir et al., 1992; Plank and Langmuir, 1992] developed a forward model of polybaric melting of passively upwelling mantle peridotite that to a first-order accounts for global variations in mid-ocean ridge basalt (MORB) major element compositions and crustal volumes. Based on MORB sodium and iron contents and crustal thicknesses, Langmuir and coworkers concluded that mantle temperatures vary by up to 250°C along the global ridge system (including Iceland). While the mantle source for the MORB system is dominantly peridotite, it is indisputable that the Earth's mantle is chemically and isotopically heterogeneous on a range of scales (including

mid-ocean ridges) [Gast *et al.*, 1964; Gast, 1968; Schilling and Winchester, 1969; Schilling, 1973] as a consequence of crust/lithosphere recycling [e.g., Zindler *et al.*, 1979; Hofmann and White, 1982; Allegre and Turcotte, 1986; Hauri, 1996; Hirschmann and Stolper, 1996; Chauvel and Hémond, 2000; Huang and Frey, 2005; Stracke, 2012], mantle metasomatism [e.g., Niu and O'Hara, 2003], formation of secondary pyroxenites from subsolidus reactions between these recycled lithologies and mantle peridotite [e.g., Herzberg, 2011], and melt-rock reactions [e.g., Sobolev *et al.*, 2005]. These more exotic mantle lithologies span a spectrum from pyroxenite, to enriched peridotite, to highly depleted harzburgite, all of which individually or collectively may dominate the melting process in some tectonic settings.

Here we fully describe, discuss enhancements to, and provide new examples of the forward model REEBOX PRO, which simulates adiabatic decompression melting of upwelling, lithologically heterogeneous mantle. The routine was developed by Brown and Lesher [2014] in their study of North Atlantic magmatism, and is here presented as a standalone executable program for Windows and Mac OSX operating systems (available for download at <http://volcano.au.dk/reebox-pro/>). The program, written and compiled in MATLAB, is suitable for modeling mantle melting in a variety of divergent margin environments where passive or active upwelling occurs. REEBOX PRO includes melting parameterizations for several lherzolite lithologies (hydrous and anhydrous pyroxenite and depleted MORB mantle peridotite), harzburgite, and pyroxenite (G2 and MIX1G compositions), and takes into account variations in mantle potential temperature and mantle flow (passive flow, melting-induced active flow [Langmuir *et al.*, 1992; Plank and Langmuir, 1992], and active flow due to intrinsic source buoyancy [Brown and Lesher, 2014]). Model outputs include melt volume (as igneous crustal thickness) and mean trace element and isotopic compositions comprising the model bulk crust, which when combined with geophysical and geochemical constraints on the volume and composition of basaltic crust, respectively, can constrain melting model parameters (and hence mantle conditions) giving rise to basaltic magmatism as shown by previous studies [McKenzie and Bickle, 1988; Langmuir *et al.*, 1992; Hirschmann and Stolper, 1996; Asimow *et al.*, 2001; Brown and Lesher, 2014; Shorttle *et al.*, 2014]. In the following section (section 2), we present background on the fundamental relations and parameters required to quantitatively model melt generation. The equations governing REEBOX PRO, and their implementations are discussed in section 3, while in the final section (section 4) we illustrate some of the model's functionality, provide benchmark tests, and highlight how model outputs can be applied "offline" to explore more nontraditional melt pooling scenarios.

## 2. Background

Quantitative models of mantle melting require melting, chemistry, and mixing functions [Langmuir *et al.*, 1992]. The *melting function* specifies the amount of melt generated per decrement of pressure (polybaric productivity of melting;  $\frac{dF}{dP}$ ) for each source lithology, and is typically quantified in one of three main ways. The first approach assumes that the polybaric productivity for each lithology is either constant or changes linearly with depth through the melting interval [e.g., Turcotte and Ahern, 1978; Klein and Langmuir, 1987; Niu and Batiza, 1991; Kinzler and Grove, 1992a; Stracke *et al.*, 2003b; Stracke and Bourdon, 2009]. Detailed thermodynamic analysis of isentropic polybaric productivity equations by Asimow *et al.* [1997], however, indicates that this approach is a gross oversimplification and not thermodynamically valid. The second approach employs internally consistent thermodynamic models that minimize free energy (e.g., pMELTS) [Ghiorso *et al.*, 2002]. However, application of such models to melting a lithologically heterogeneous source is not without significant challenges and limitations [see Rudge *et al.*, 2013]. The third approach utilizes thermodynamic expressions for polybaric productivity that incorporate parameterizations of high pressure melting experiments. Although to date this is the most common approach for both lithologically homogeneous and heterogeneous mantle sources [e.g., McKenzie and Bickle, 1988; Iwamori *et al.*, 1995; Katz *et al.*, 2003; Ito and Mahoney, 2005; Brown and Lesher, 2014; Kimura and Kawabata, 2014; Shorttle *et al.*, 2014; Kimura and Kawabata, 2015], it suffers from a paucity of experimental data on the full range of lithologies likely to be present in the mantle.

The *chemistry function* quantifies the compositions of the instantaneous melts generated from each source during each decompression step, and depends upon the style in which melt is extracted from the mantle. It is widely agreed that under most conditions of decompression melting melt is removed from equilibrium with the solid as soon as it forms [e.g., McKenzie, 1985; Johnson *et al.*, 1990] and thus the process can be

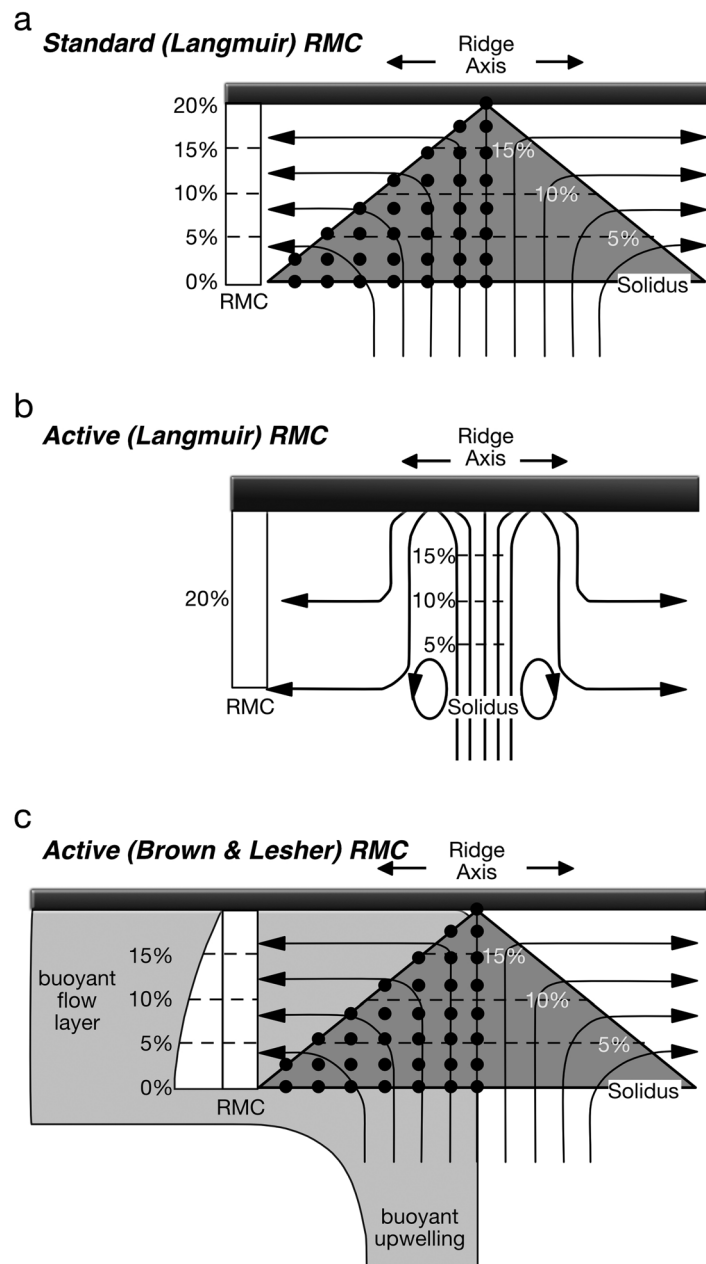


**Figure 1.** Residual mantle columns (RMC) for different melting scenarios included in REE-BOX PRO. (a) Standard (Langmuir) RMC assumes incremental batch melting (black circles), and passive upwelling, which results in a residual mantle column exiting the sides of the melting zone per unit spreading. Individual solid mantle flow paths (black curves with arrows) define melting columns of different length, resulting in a roughly triangular shape to the melting zone (dark grey-shaded region). (b) Active (Langmuir) RMC assumes the end-member case of melting-related active upwelling within the melting zone. All solid-mantle flow paths decompress to the base of the lithosphere. (c) Active (Brown and Lesher) RMC [Brown and Lesher, 2014], where a residual mantle cylinder caused by active flow due to source buoyancy is added to the standard residual mantle column formed by passive upwelling. Black circles same as in Figure 1a. Percentage contours indicate the total extent of melting. Figures 1a and 1b after Plank and Langmuir [1992].

etry defined by several melting columns of different length (Figure 1a). Thus, the mixing function should also account for these different length melting columns and the two-dimensional nature of the flow (cornerflow) [Klein and Langmuir, 1987; Spiegelman and McKenzie, 1987; McKenzie and Bickle, 1988; Langmuir et al., 1992; Asimow et al., 2001].

modeled as near-fractional fusion [Shaw, 1970], incremental batch melting [Wood, 1979], or dynamic melting (where some critical melt fraction remains in equilibrium with the residual solid, while greater amounts are instantaneously removed) [Langmuir et al., 1977; McKenzie, 1985].

The *mixing function* describes how instantaneous melts within the melting zone are aggregated to form the mean composition and volume of the igneous crust derived from the melting zone. In many mantle melting models, aggregate melt compositions are calculated by mixing instantaneous melts along a single melting column only [Niu and Batiza, 1991; Herzberg et al., 2005; Stracke and Bourdon, 2009; Koornneef et al., 2012]. This single melting column represents the longest melting path beneath the lithosphere, and may be applicable for cases of intraplate melting and end-member active flow beneath mid-ocean ridges driven by buoyancy effects due to melt depletion and/or melt retention [Plank and Langmuir, 1992; Shen and Forsyth, 1995; Asimow et al., 2001]. However, for many divergent margin environments, upwelling mantle interacts with the lithosphere and the solid mantle flow paths become horizontal with increasing depth away from the upwelling axis (i.e., ridge/rift axis in divergent margin environments). Because melting only occurs along decompression paths, the horizontal component of flow will result in a mantle melting zone with a roughly triangular geom-

In accounting for 2-D flow beneath mid-ocean ridges, Langmuir and coworkers [Langmuir *et al.*, 1992; Plank and Langmuir, 1992; Plank *et al.*, 1995] noted that the effects of this flow are preserved by the column of mantle residues that laterally exit the melting zone (Figure 1) because this “residual mantle column” (RMC) provides a record of all mantle flow paths through the melting zone. Residues following the shortest flow paths (i.e., lowest degrees of melting) are preserved at the bottom, whereas residues following the longest melting paths (largest degrees of melting) are preserved at the top of the RMC [Langmuir *et al.*, 1992]. The shape of the RMC describes the relative depth-dependent weighting of melts to the final mixture comprising the bulk crust, and is a function of the rate at which the solid residue exits the melting zone at any given depth, as governed by the mantle flow field. For example, passive upwelling results in a flow field where the solid residue exits the melting zone at the same velocity at *all* depths (generally equivalent to the half-spreading rate), producing a residual mantle “column” (e.g., Figure 1a). However, Ito and Mahoney [2005] noted that buoyancy-driven flow due to thermal and/or compositional factors can lead to nonuniform rates of flow through the melting zone. These authors quantified such dynamic flow beneath stationary lithosphere using lubrication theory (thin-layer flow), and showed that the dynamic flow velocities exiting the melting zone are highest at the base of the buoyant layer and decline to zero at the base of the lithosphere. Such a flow field produces a residual mantle column that gives greater weighting to deeply derived melts. Ito and Mahoney [2005] referred to this RMC as the residual melting “cylinder,” although strictly speaking the treatment is still for two dimensions.

A final consideration for a mixing function appropriate to lithologically heterogeneous mantle is the fact that pyroxenites or their partial melts can react with the host peridotite to form hybrid lithologies [Kogiso *et al.*, 2004; Sobolev *et al.*, 2005; Herzberg, 2011]. Such reactions may result in a full range of pyroxenite to peridotite lithologies that are potentially involved in the melting process. For example, some pyroxenite bulk compositions are silica-deficient (i.e., plot to the olivine side of the pyroxene-garnet plane in the forsterite—Ca-Tschermaks—quartz—diopside normative system) [O’Hara, 1968], and can contain olivine [e.g., Hirschmann and Stolper, 1996; Kogiso and Hirschmann, 2006; Herzberg, 2011]. Partial melts derived from such pyroxenites are silica-undersaturated and can mingle and mix with partial melts of peridotite to generate basalt [Hirschmann *et al.*, 2003; Herzberg, 2011]. However, other pyroxenite bulk compositions (including recycled mid-ocean ridge basalt) are silica-saturated (i.e., plot to the quartz side of the pyroxene-garnet plane in the forsterite—Ca-Tschermaks—quartz—diopside normative system) [O’Hara, 1968], and contain quartz and/or its high pressure polymorphs [e.g., Hirschmann and Stolper, 1996; Kogiso and Hirschmann, 2006; Herzberg, 2011]. Because such lithologies and their partial melts are silica-saturated, reactions can take place between these pyroxenites (and/or their partial melts) and the surrounding mantle peridotite to form secondary, hybrid pyroxenite lithologies [Kogiso *et al.*, 2004; Sobolev *et al.*, 2005; Herzberg, 2011; Lambart *et al.*, 2012]. Furthermore, because partial melting of these hybrid lithologies can yield silica-rich melts, mingling of hybrid pyroxenite melts with peridotite partial melts will not create basalt, but may crystallize to form a different pyroxenite lithology [Herzberg, 2011]. Presently it is extremely difficult to quantitatively model such lithologic diversity [Sobolev *et al.*, 2005; Katz and Rudge, 2011; Katz and Weatherley, 2012; Kimura and Kawabata, 2015], although forward modeling such as presented here can offer insights into the significance of such lithological variability on the composition and volume of basalt produced by decompression melting.

### 3. REEBOX PRO Overview and Governing Equations

REEBOX PRO is a standalone, compiled MATLAB application, and employs a graphical user interface. *The user does not need MATLAB to be installed on their computer, nor do they need knowledge of MATLAB coding to use REEBOX PRO.* The program simulates adiabatic decompression melting assuming incremental batch melting, and uses thermodynamic constraints for melting a lithologically heterogeneous source developed in Brown and Lesher [2014]. The model takes as inputs user-specified values for mantle potential temperature ( $T_p$ ), half-spreading rate, thickness of any preexisting mechanical boundary layer (e.g., continental lithosphere if modeling continental breakup), and abundance and initial trace element (Rb, Ba, Th, U, Nb, Ta, K, La, Ce, Pb, Pr, Sr, Nd, Sm, Zr, Hf, Eu, Ti, Gd, Dy, Y, Er, Yb, and Lu) and isotopic ( $^{87}\text{Sr}/^{86}\text{Sr}$ ,  $^{143}\text{Nd}/^{144}\text{Nd}$ ,  $^{176}\text{Hf}/^{177}\text{Hf}$ , and  $^{206}\text{Pb}/^{204}\text{Pb}$ ) compositions for up to and including five lithologies that span the range of compositions inferred for the mantle, including anhydrous peridotite, hydrous peridotite, harzburgite, and silica saturated

and undersaturated pyroxenite. Whereas most peridotite melting parameterizations commonly assume a fertile (pyrolitic) peridotite composition [e.g., *Katz et al.*, 2003], REEBOX PRO can also simulate melting of a more depleted peridotite composition (i.e., higher proportions of olivine and orthopyroxene and lower proportions of clinopyroxene than pyrolite at any given pressure) given that the mantle source for mid-ocean ridge magmatism (depleted MORB mantle; DMM) is typically more depleted than pyrolite [*Salters and Stracke*, 2004; *Workman and Hart*, 2005].

For each specified lithology, the program outputs the compositions of melts generated during each decompression step (instantaneous melts), the compositions of instantaneous melts accumulated along the longest solid-mantle flow line through the melting zone (column-accumulated melts), and the compositions of melts accumulated along all mantle flow lines through the melting zone (pooled melts). The program also outputs the mean trace element and isotopic compositions and thickness of the bulk igneous crust derived by mixing all pooled melts from the specified lithologies. Given the variety of possible mantle flow fields in divergent margins settings, the program allows the user to calculate bulk crust properties for the cases of passive upwelling, active upwelling induced by melting effects [e.g., *Sotin and Parmentier*, 1989], and active upwelling due to intrinsic buoyancy in the source due to thermal and/or compositional effects [*Ito and Mahoney*, 2005; *Brown and Leshner*, 2014]. Furthermore, if the user's modeling scenario is not consistent with these cases, REEBOX PRO outputs can be used to construct different mixing calculations "off-line" (see section 4.3). Finally, the overall architecture of REEBOX PRO has been designed for future integration into fully dynamical models of mantle flow and such enhancements will be included in future releases. The current executable (standalone) version of REEBOX PRO released with this publication can be downloaded at <http://volcano.au.dk/reebox-pro/>, and a user's guide is provided in the supporting information. We present the key equations below.

### 3.1. REEBOX PRO Melting Functions

Because REEBOX PRO simulates melting of a lithologically heterogeneous mantle source containing lithologies having different melting behaviors, it is essential to distinguish at any given time in the melting process those lithologies that are melting from those that are not melting. Consider  $k$  lithologies (indexed by  $l$ ), of which, at any given time,  $m$  are melting (indexed by  $i$ ) and  $n$  are not (indexed by  $j$ ), such that

$$\sum_l^k \Phi_l^0 = \sum_i^m \Phi_i^0 + \sum_j^n \Phi_j^0 = 1, \quad (1)$$

where  $\Phi_i^0$  and  $\Phi_j^0$  are the initial mass fractions of lithologies  $i$  and  $j$ , respectively.

Assuming that all specified source lithologies are in thermal (but not chemical) equilibrium, decompression melting can be simulated as an isentropic (i.e., adiabatic and reversible) process for both lithologically homogeneous and heterogeneous sources [*McKenzie*, 1984; *Iwamori et al.*, 1995; *Asimow et al.*, 1997; *Phipps Morgan*, 2001; *Stolper and Asimow*, 2007]. (Note that for fractional melting, this process must be simulated incrementally (termed "incrementally isentropic" fractional fusion) because melt extraction removes entropy from the system [see *Asimow et al.*, 1997; *Stolper and Asimow*, 2007 for details]. Consequently, all of the thermally equilibrated lithologies must follow the same pressure-temperature path upon decompression, and the melting rates of the individual lithologies are governed by the entropy budget of the combined lithologic assemblage [e.g., *Phipps Morgan*, 2001; *Stolper and Asimow*, 2007]. An important consequence of lithologic heterogeneity in isentropic decompression melting is that heat flows from the nonmelting lithologies into the melting lithologies, increasing melt production rates in the melting lithologies, and cooling the nonmelting lithologies such that they cross their solidi much shallower (if at all) than they would if they each comprised a single homogeneous source [*Sleep*, 1984; *Hirschmann and Stolper*, 1996; *Phipps Morgan*, 2001; *Stolper and Asimow*, 2007; *Katz and Rudge*, 2011].

Because REEBOX PRO simulates incremental batch melting with complete melt withdrawal, the program computes polybaric melt productivities for the  $k$  lithologies using the equation for incrementally isentropic fractional melting derived by *Brown and Leshner* [2014]. Thus, melting of, for example, lithology  $i = 1$  is

$$-\left(\frac{dF_1}{dP}\right)_S = \frac{\left\{ \begin{aligned} &\sum_i^m \left( \Phi_i^0 (1-F_i) \left[ \left(\frac{C_p^S}{T}\right) \left(\frac{\partial T_1}{\partial P}\right)_{F_i} - \alpha^S \right] \right) \\ &+ \sum_{i=2}^m \left( \Phi_i^0 \Delta S_{fusion_i} \left[ \left(\frac{\partial T_1}{\partial P}\right)_{F_i} - \left(\frac{\partial T_i}{\partial P}\right)_{F_i} \right] \right) \\ &+ \sum_j^n \left( \Phi_j^0 \left[ \left(\frac{C_p^S}{T}\right) \left(\frac{\partial T_1}{\partial P}\right)_{F_i} - \alpha^S \right] \right) \end{aligned} \right\}}{\left\{ \begin{aligned} &\Phi_1^0 \Delta S_{fusion_1} + \sum_i^m \left( \Phi_i^0 (1-F_i) \left[ \left(\frac{C_p^S}{T}\right) \left(\frac{\partial T_1}{\partial F_1}\right)_P \right] \right) \\ &+ \sum_{i=2}^m \left( \Phi_i^0 \Delta S_{fusion_i} \left[ \left(\frac{\partial T_1}{\partial F_1}\right)_P \right] \right) + \sum_j^n \left( \Phi_j^0 \left[ \left(\frac{C_p^S}{T}\right) \left(\frac{\partial T_1}{\partial F_1}\right)_P \right] \right) \end{aligned} \right\}}. \quad (2)$$

The subscript *S* on the derivative on the left side of equation (2) denotes an isentropic process. This derivative is negative because the extent of melting increases with decreasing pressure. Equation (2) contains several standard thermodynamic quantities: isobaric heat capacity of the solid,  $C_p^S$ , coefficient of thermal expansion of the solid,  $\alpha^S$ , temperature,  $T$ , and the bulk source density,  $\rho^S$  (the details of how this is calculated are provided below). The remaining variables are the change in entropy during melting for each lithology,  $\Delta S_{fusion_i}$ , and the total mass fraction of melt derived from the melting lithology,  $F_i$  (see Table 1 for all model parameters). Briefly, the variables in the numerator and denominator are organized in terms of the melting lithologies ( $\sum_i^m$  and  $\sum_{i=2}^m$  terms), the nonmelting lithologies ( $\sum_j^n$  terms), and the melting lithology being considered (lithology  $i = 1$ ;  $\Phi_1^0 \Delta S_{fusion_1}$  term in the denominator). See *Brown and Lesher* [2014] for more details.

The change in temperature during melting (in this case, in terms of melting lithology  $i = 1$ ) [*Phipps Morgan*, 2001] is

$$\left(\frac{dT}{dP}\right)_S = \left(\frac{\partial T_1}{\partial P}\right)_{F_1} + \left(\frac{\partial T_1}{\partial F_1}\right)_P \left(\frac{dF_1}{dP}\right)_S. \quad (3)$$

To explicitly calculate  $F$  and  $T$  at a specific  $P$  as melting progresses, equations (2) and (3) are integrated simultaneously using the fourth-order Runge-Kutta method [*Press et al.*, 1992]. The partial derivatives,  $\left(\frac{\partial T}{\partial P}\right)_F$  and  $\left(\frac{\partial T}{\partial F}\right)_P$ , in equations (2) and (3) capture the melting behavior of all lithologies crossing their solidi. These partial derivatives are evaluated using finite difference on parameterizations of high  $P$  melting experiments relating  $T$ ,  $F$ , and  $P$  for a given lithology. For anhydrous and hydrous peridotite, and harzburgite we utilized modified versions of the parameterizations presented by *Katz et al.* [2003]. For silica-saturated pyroxenite, we use the parameterization for the G2 bulk composition of *Pertermann and Hirschmann* [2003a], while for silica-undersaturated pyroxenite we have developed a new parameterization based upon the melting experiments for MIX1G pyroxenite performed by *Hirschmann et al.* [2003] and *Kogiso et al.* [2003]. Details of these parameterizations are provided in Appendix A.

To illustrate the functionality of equations (2) and (3) and how they capture the thermal behavior of both lithologically homogeneous and heterogeneous systems, we compare the melting behavior for a potential temperature of 1450°C under end-member conditions in Figure 2, where the polybaric productivity is plotted as a function of pressure. The first is for melting a series of homogeneous sources, each composed entirely of one of the possible source lithologies incorporated in REEBOX PRO (for hydrous melting we consider only the case for 500 ppm H<sub>2</sub>O). The second example is for the melting of a heterogeneous source containing 20% of each lithology. A couple of features are noteworthy in Figure 2. First, for the hypothetical case where each lithology is considered separately (i.e., each is modeled as a homogeneous single-lithology source), the maximum polybaric productivity ranges from a low of ~9.9%/GPa for hydrous peridotite to a high of ~16%/GPa for G2 pyroxenite (Figure 2a). In contrast, for the hypothetical heterogeneous source

**Table 1.** REEBOX PRO Model Parameters<sup>a</sup>

Variable	Description	Default Value	Units	Reference
$\Phi_i^0$	Initial mass fraction of melting lithology			
$\Phi_j^0$	Initial mass fraction of nonmelting lithology			
$\Phi^0$	Initial mass fraction of any lithology			
$\rho^S$	Bulk density of mantle source		$\text{kg m}^{-3}$	
$\rho_{crust}$	Basaltic crust density	2800	$\text{kg m}^{-3}$	
$\rho_0$	Ambient mantle density		$\text{kg m}^{-3}$	
$\rho_{CC}$	Continental crust density	2700	$\text{kg m}^{-3}$	
$\rho_{LM}$	Lithospheric mantle density	3300	$\text{kg m}^{-3}$	
$\Delta\rho$	Net density deficit of source		$\text{kg m}^{-3}$	
$C_p^S$	Isobaric specific heat capacity	1200	$\text{J kg}^{-1}\text{K}^{-1}$	<i>Phipps Morgan</i> [2001]
$\alpha^S$	Coefficient of thermal expansion	$3 \times 10^{-5}$	$\text{K}^{-1}$	<i>Sleep</i> [1990]
$\Delta S_{fusion,i}$	Entropy change during melting of peridotite/harzburgite	300	$\text{J kg}^{-1}\text{K}^{-1}$	<i>Katz et al.</i> [2003]
$\Delta S_{fusion,j}$	Entropy change during melting of G2 pyroxenite/MIX1G pyroxenite	240	$\text{J kg}^{-1}\text{K}^{-1}$	<i>Ito and Mahoney</i> [2005]
$F_i$	Total mass fraction of melt of lithology <i>i</i>			
$dF_i^*$	Mass fraction of melt generated from lithology <i>i</i> during decompression step			
$F_B$	Mean extent of melting			
$g$	Acceleration due to gravity	9.8	$\text{m s}^{-2}$	
$T_P$	Mantle potential temperature		$^{\circ}\text{C}$	
$T_P^0$	Ambient mantle potential temperature		$^{\circ}\text{C}$	
$T$	Temperature		K	
$T_{base}^{real}$	Temperature at base of melting zone		K	
$T_{ref}^{real}$	Temperature of adiabat at reference pressure		K	
$P$	Pressure		Pa	
$P_0$	Initial pressure of melting or pressure at base of horizontal flow layer	see text	Pa	
$P_f$	Final pressure of melting		Pa	
$P_{base}$	Pressure at base of melting zone		Pa	
$P_{ref}$	Reference pressure	$6.75 \times 10^9$	Pa	
$P_{flow}$	Pressure at base of buoyant horizontal flow layer		Pa	
$P_{crust}$	Pressure at base of igneous crust		Pa	
$p_{pre-existing lithosphere}$	Pressure at base of pre-existing lithosphere		Pa	
$\eta$	Mantle viscosity		Pa-s	
$\eta_0$	Reference viscosity	$1 \times 10^{20}$	Pa-s	<i>Brown and Lesher</i> [2014]
$E_{act}$	Activation energy	$1.9 \times 10^5$	$\text{J mol}^{-1}$	<i>Ito et al.</i> [1999]
$V_{act}$	Activation volume	$4 \times 10^{-6}$	$\text{m}^3 \text{mol}^{-1}$	<i>Ito et al.</i> [1999]
$R_{ideal}$	Ideal gas constant	8.314	$\text{J mol}^{-1} \text{K}^{-1}$	
$R$	Radius of buoyant upwelling		m	
$B$	Upwelling buoyancy flux		$\text{kg s}^{-1}$	
$Q$	Upwelling volume flux		$\text{m}^3 \text{s}^{-1}$	
$U_0$	Half-spreading rate		m/s	
$U(P)$	Pressure-dependent horizontal flow			
$u_x^{active}(P)$	Pressure-dependent horizontal flow due to active upwelling		$\text{m s}^{-1}$	
$u_z^{active}(P)$	Pressure-dependent vertical flow due to active upwelling		$\text{m s}^{-1}$	
$\bar{u}_x^{-active}$	Mean horizontal velocity due to buoyant flow		$\text{m s}^{-1}$	
$\bar{u}_z^{-active}$	Mean upwelling velocity due to buoyant flow		$\text{m s}^{-1}$	
$X_i^{\Psi}$	Modal abundance of phase $\Psi$ in lithology <i>i</i>			
$y_i^{\Psi}$	Melting reaction coefficient for phase $\Psi$ in lithology <i>i</i>			
$k_{d,i}^{\Psi}$	Mineral-melt partition coefficient for element in phase $\Psi$ in lithology <i>i</i>			
$p_i$	Bulk distribution coefficient for minerals contributing to melt from lithology <i>i</i>			
$D_i$	Bulk distribution coefficient for element in lithology <i>i</i>			
$H_{lithosphere}$	Preexisting lithosphere thickness		m	
$H_{crust}$	Thickness of igneous crust derived from either the standard (Langmuir) or active (Brown and Lesher) RMC		m	
$H_{crust}^{activeRMC(Langmuir)}$	Thickness of igneous crust derived from active (Langmuir) RMC		m	
$H_{flow}$	Characteristic thickness of buoyant horizontal flow		m	
$f_{crust}$	Mass fraction of crust in preexisting lithosphere	0.3		
$c_i$	Instantaneous elemental concentration in melt derived from lithology <i>i</i>		ppm	
$c_i^{residue}$	Elemental concentration in residue of lithology <i>i</i>		ppm	
$c_i^I$	Instantaneous elemental concentration for element corresponding to isotope		ppm	
$C$	Mean elemental concentration of igneous crust derived from either the standard (Langmuir) or active (Brown and Lesher) RMC		ppm	

Table 1. (continued)

Variable	Description	Default Value	Units	Reference
$I$	Mean isotopic composition of igneous crust derived from either the standard (Langmuir) or (active) Brown and Lesher RMC			
$I_i$	Isotopic composition of lithology $i$			
$C_i^{mf}$	Mantle flow path-averaged concentration for element corresponding to isotope		ppm	
$\bar{C}^{activeRMC(Langmuir)}$	Mean elemental concentration of igneous crust derived from active (Langmuir) RMC			
$\bar{I}^{activeRMC(Langmuir)}$	Mean isotopic composition of igneous crust derived from active (Langmuir) RMC			

<sup>a</sup>To provide the most flexibility, most model parameters can be adjusted by the user in REEBBOX PRO, including the thermodynamic parameters governing melting (equation (2)), viscosity parameters governing flow using the active (Brown and Lesher) RMC mixing function (equation (20)), and the parameters governing the pressure at the base of preexisting lithosphere (equation (27)).

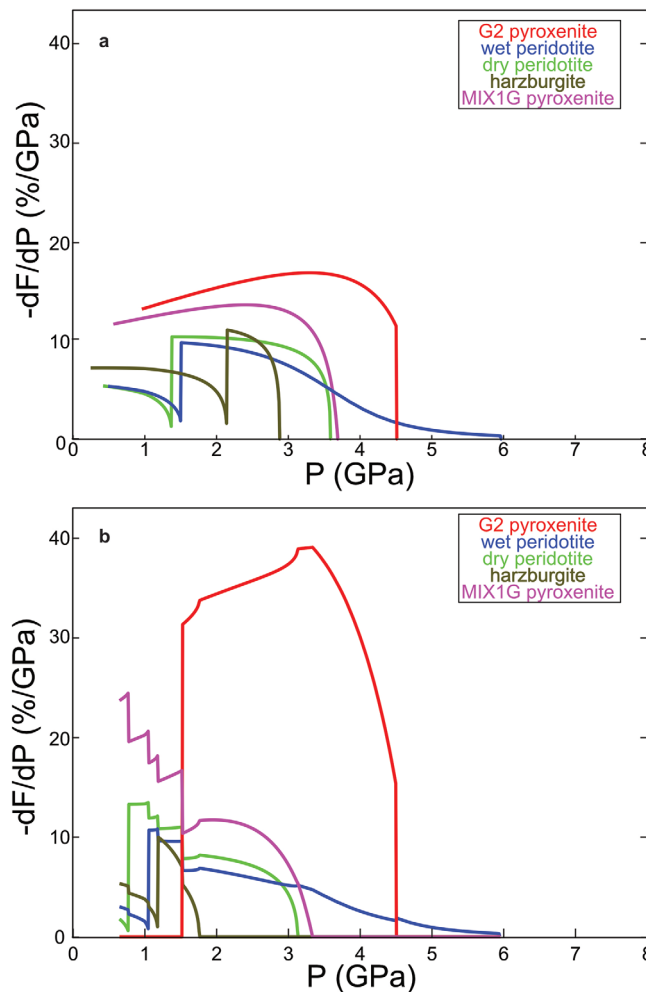


**Figure 2.** Melting functions for  $T_p = 1450^\circ\text{C}$  for hypothetical source conditions. (a) Melting functions for anhydrous peridotite, hydrous peridotite (500 ppm  $\text{H}_2\text{O}$ ), harzburgite, G2 pyroxenite, and MIX1G pyroxenite, assuming each is melting as a homogeneous (single lithology) mantle source. The kinks in the anhydrous peridotite, hydrous peridotite, and harzburgite curves correspond to the exhaustion of clinopyroxene from the residue. (b) Melting functions for a heterogeneous source containing 20% each of anhydrous peridotite, hydrous peridotite (500 ppm  $\text{H}_2\text{O}$ ), harzburgite, G2 pyroxenite, and MIX1G pyroxenite.

containing 20% of each of the lithologies, the maximum polybaric productivity differs greatly (Figure 2b). In this case, the maximum productivity for G2 pyroxenite is  $\sim 39\%/GPa$ , and before G2 pyroxenite is exhausted the polybaric productivity for harzburgite never reaches more than  $4\%/GPa$ . Similar behavior can be seen for other lithologies during the early melting of G2 pyroxenite—a direct consequence of the net heat transfer into the melting lithologies from the nonmelting lithologies. Second, this transfer of heat from the nonmelting to melting lithologies at higher pressures in the heterogeneous source example causes MIX1G pyroxenite, dry peridotite, and harzburgite to begin melting more shallowly than they would if they were homogeneous sources (Figures 2a and 2b). Finally, melting of hydrous peridotite involves a low-productivity tail compared to anhydrous melting (Figure 2a) that results in lower maximum melt productivity of the hydrous source compared to the anhydrous source [e.g., *Asimow and Langmuir, 2003*].

### 3.2. REEBBOX PRO Chemistry Functions

Instantaneous melt compositions for each source lithology are calculated assuming nonmodal incremental batch melting during each decompression step [*Shaw, 1970*]

$$c_i = \frac{c_i^{residue}}{dF_i^*(1-p_i) + D_i} \quad (4)$$

The concentration of any trace element derived from lithology  $i$  in the instantaneous melt ( $c_i$ ) depends upon the mass fraction of melt generated during the decompression step ( $dF_i^*$ ), the concentration of the element in the residue ( $c_i^{residue}$ ), the bulk distribution coefficient for the element ( $D_i$ ), and the bulk distribution coefficient for the minerals contributing to the melt ( $p_i$ ). The mass fraction of melt generated during each decompression step is given by the melting function (equation (2)), and the element concentrations in the residue are [Shaw, 1970]

$$c_i^{residue} = \left( \frac{D_i - p_i dF_i^*}{1 - dF_i^*} \right) \left( \frac{c_i^{residue-1}}{dF_i^*(1-p_i) + D_i} \right), \quad (5)$$

where  $c_i^{residue-1}$  is the concentration of the trace element in the residue after the *previous* melting step. The elemental partitioning variables,  $D_i$  and  $p_i$ , are

$$D_i = \sum x_i^\Psi k_{d_i}^\Psi, \quad (6)$$

and

$$p_i = \sum y_i^\Psi k_{d_i}^\Psi, \quad (7)$$

respectively, where,  $k_{d_i}^\Psi$  is the mineral-melt partition coefficient for any given element in solid phase  $\Psi$  in lithology  $i$ ,  $x_i^\Psi$  is the modal abundance of any given solid phase in lithology  $i$ , and  $y_i^\Psi$  is the melting reaction stoichiometry for any given solid phase in lithology  $i$ . Model outputs include the instantaneous melt compositions for all melting lithologies, as calculated using equation (4).

To quantify the modal abundances ( $x_i^\Psi$ ) and melting reaction coefficients ( $y_i^\Psi$ ) in the above equations, we have developed new parameterizations for mineral mode abundances as a function of pressure and melt depletion for all modeled lithologies (details are provided in Appendix B). For peridotite, we have parameterized available experimental information for pyrolite (MM3 and Kettle River bulk compositions) [Baker and Stolper, 1994; Walter, 1998], and have modified these parameterizations to simulate the evolution of mineral modes and melting reaction coefficients for depleted lherzolite (DMM) [Workman and Hart, 2005] and harzburgite. For G2 and MIX1G pyroxenites, we assume biminerally assemblages of clinopyroxene and garnet, and constrain their melting modes from experiments by Hirschmann and coworkers [Hirschmann et al., 2003; Kogiso et al., 2003; Pertermann and Hirschmann, 2003a,b]. The parameterizations are programmed in REEBOX PRO as look-up tables of modal abundance and melting reaction coefficient at specific  $P$  and  $F$  between 1–7 GPa and 0–100%  $F$ , respectively. REEBOX PRO interpolates the mineral modes and melting reactions from these look-up tables using the  $P$  and  $F$  derived from the melting functions (equation (2)). An advantage of implementing look-up tables for the melting reaction coefficients is that changes in melting reactions associated with phase-in and phase-out boundaries are easily accounted for.

For mineral-melt partitioning ( $k_d^\Psi$ ) during anhydrous/hydrous peridotite and harzburgite melting, REEBOX PRO utilizes the temperature-dependent mineral-melt partition coefficient parameterizations of Kimura and Kawabata [2014] for orthopyroxene, clinopyroxene, and garnet. Because these authors have not included spinel in their parameterizations, we utilize mineral-melt partition coefficients for spinel compiled from the literature [McKenzie and O'Nions, 1991; Horn et al., 1994; McKenzie and O'Nions, 1995; Klemme et al., 2006]. For simplicity, we do not consider the aluminous phase transition from spinel to plagioclase at  $P < 1$  GPa in the peridotite lithologies. Finally, we have developed a new temperature-dependent parameterization for olivine-melt partitioning based on lattice-strain theory (see Appendix C) that differs from the melt composition-based partitioning proposed by Kimura and Kawabata [2014].

To provide maximum flexibility for the user, we have incorporated options to use the temperature-dependent partition coefficients, a set of peridotite mineral-melt partition coefficients compiled from the literature [McKenzie and O'Nions, 1991; Horn et al., 1994; Salters and Stracke, 2004; Klemme et al., 2006; Pilet et al., 2011] (see Table C2) or the option to input values of one's choosing. A comparison of the parameterized temperature-dependent mineral-melt partition coefficients and the compiled mineral-melt partition coefficients (Table C2) is shown in Figure 3, where it can be seen that the two different methods result in generally similar bulk distribution coefficients.

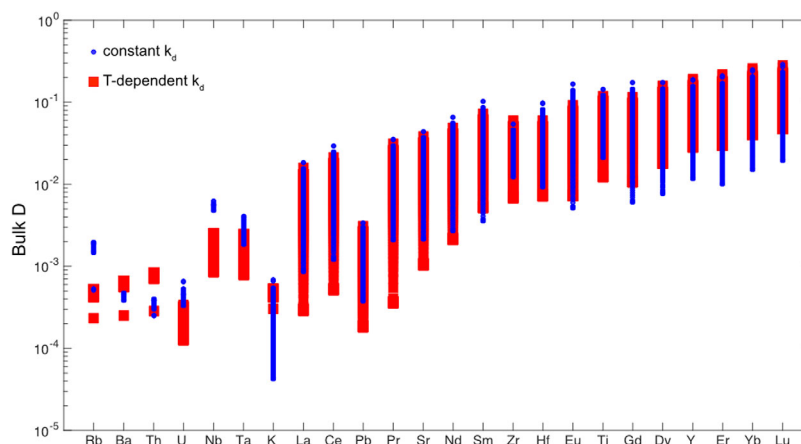


**Figure 3.** Peridotite bulk mineral-melt partition coefficients ( $D$ ) using  $T$ -dependent coefficients (red) and constant values from Table C2 (blue), calculated for a fertile peridotite source having a potential temperature of  $1400^{\circ}\text{C}$  (solidus is within the garnet stability field). The ranges of the values shown for each element reflect the change in the bulk distribution coefficient as the residual mineral mode (constant  $k_d$ ) or residual mineral mode and temperature ( $T$ -dependent  $k_d$ ) evolve during melting.

Data for eclogite/pyroxenite mineral-melt partition coefficients are scant, and thus we use the experimentally determined partition coefficients from *Pertermann et al.* [2004] and *Klemme et al.* [2002] for all decompression steps (Table C3). As for peridotite, REEBOX PRO gives the option to input user-preferred partition coefficients for pyroxenite.

### 3.3. REEBOX PRO Mixing Functions

The mixing function combines the melting and chemistry functions to calculate the composition and volume (thickness) of the bulk igneous crust. Assuming complete extraction of all melt generated within the melting zone, the REEBOX PRO mixing function employs the residual mantle column framework because it can be applied to a variety of melt pooling scenarios and mantle flow fields [e.g., *Ito and Mahoney*, 2005; *Brown and Lesher*, 2014]. Given this flexibility, REEBOX PRO allows the user the option to calculate mean crustal properties for three distinct flow fields, including

1. passive upwelling and uniform horizontal flow through the entire melting zone, which is quantified using the “standard” residual mantle column calculation [*Langmuir et al.*, 1992; *Plank and Langmuir*, 1992] (hereafter referred to as “standard (Langmuir) RMC”);
2. end-member active upwelling, which assumes that all melting columns in the melting zone decompress to the base of the lithosphere as a result of enhanced buoyancy due to melt depletion of the mantle residue and/or melt retention, which is quantified using the “active” residual mantle column calculation [*Langmuir et al.*, 1992; *Plank and Langmuir*, 1992] (hereafter referred to as “active (Langmuir) RMC”);
3. passive upwelling combined with active upwelling induced by intrinsic source buoyancy, which is quantified by combining the residual mantle column [*Langmuir et al.*, 1992; *Plank and Langmuir*, 1992] and residual mantle cylinder [*Ito and Mahoney*, 2005] calculations [*Brown and Lesher*, 2014] (hereafter referred to as “active (Brown and Lesher) RMC”).

These scenarios are shown schematically in Figure 1. Given current limitations on modeling the interactions between peridotite and pyroxenite and pyroxenite-derived melts, REEBOX PRO does not consider the formation of hybrid lithologies [see also *Brown and Lesher*, 2014].

Independent of which mixing function is specified, the melting and chemistry functions are related by integrating all instantaneous melts generated along each flow path at the edges of the melting zone where the flow path exits the melting zone (column-accumulated melts). The composition of melt aggregated along each flow line is quantified by

$$C_i^* = \frac{1}{F_i} \int_0^{F_i} c_i dF_i^*, \quad (8)$$

where  $c_i$  and  $dF_i^*$  were defined in equation (4), and  $F_i = \sum dF_i^*$  is the total mass fraction of melt generated along the flow path (from the melting function).

**3.3.1. Active (Langmuir) RMC Mixing Function**

We start first with the active RMC (Langmuir) mixing function because it follows from equation (8). This mixing function quantifies the mean trace element composition of the bulk crust ( $\bar{C}^{activeRMC(Langmuir)}$ ) by assuming all melting columns melt to the same maximum extent,  $F_i^{max}$ , beneath the crust/lithosphere (i.e., the mean extent of melting of the source is equivalent to  $F_i^{max}$ ),

$$\bar{C}^{activeRMC(Langmuir)} = \frac{\sum_i^m \Phi_i^0 \int_0^{F_i^{max}} c_i dF_i^*}{\sum_i^m \Phi_i^0 F_i^{max}} \tag{9}$$

The isotopic composition of the bulk crust is

$$\bar{I}^{activeRMC(Langmuir)} = \frac{\sum_i^m \Phi_i^0 I_i \int_0^{F_i^{max}} c_i^I dF_i^*}{\sum_i^m \Phi_i^0 \int_0^{F_i^{max}} c_i^I dF_i^*} \tag{10}$$

where  $F_i^{max}$  is the maximum extent of melting,  $I_i$  is the radiogenic isotopic ratio, and  $c_i^I$  is the instantaneous melt composition (equation (4)) of the element corresponding to the isotope of interest (e.g., Nd for  $^{143}\text{Nd}/^{144}\text{Nd}$ ), respectively, for lithology  $i$ . Finally, the crustal thickness is

$$H_{crust}^{activeRMC(Langmuir)} = \frac{\sum_i^m \Phi_i^0 (P_{0i} - P_f) F_i^{max}}{\rho_{crust} g} \tag{11}$$

where  $(P_{0i} - P_f)$  is the pressure difference between the bottom ( $P_{0i}$ ) and top of the melting zone (final pressure of melting,  $P_f$ ) for lithology  $i$ ,  $\rho_{crust}$  is the density of the basaltic crust, and  $g$  is the acceleration due to gravity.

**3.3.2. Standard (Langmuir) RMC and Active (Brown and Lesher) RMC Mixing Functions**

Application of the other mixing functions (standard (Langmuir) RMC and active (Brown and Lesher) RMC) requires an additional step to calculate pooled melt compositions and crustal thickness. In these cases, the mean trace element and isotopic composition of the modeled bulk crust are calculated using the same form of the mixing function, which, for a heterogeneous source, is presented by *Ito and Mahoney* [2005]. The mean composition of any trace element,  $\bar{C}$ , in the model bulk crust therefore is

$$\bar{C} = \frac{\sum_i^m C_i^* \Phi_i^0 \int_{P_{0i}}^{P_f} F_i(P) U(P) dP}{\sum_i^m \Phi_i^0 \int_{P_{0i}}^{P_f} F_i(P) U(P) dP} \tag{12}$$

and the mean isotopic composition ( $^{176}\text{Hf}/^{177}\text{Hf}$ ,  $^{143}\text{Nd}/^{144}\text{Nd}$ ,  $^{87}\text{Sr}/^{86}\text{Sr}$ ,  $^{206}\text{Pb}/^{204}\text{Pb}$ ) is

$$\bar{I} = \frac{\sum_i^m I_i C_i^* \Phi_i^0 \int_{P_{0i}}^{P_f} F_i(P) U(P) dP}{\sum_i^m C_i^* \Phi_i^0 \int_{P_{0i}}^{P_f} F_i(P) U(P) dP} \tag{13}$$

In these equations,  $F_i(P)$  is the total mass fraction of melting (at the specified pressure),  $C_i^*$  is the average composition of melts aggregated along individual flow lines through the melting zone (equation (8)),  $I_i$  is

the isotope ratio, and  $C_i^{*l}$  is the concentration of the element corresponding to the isotope of interest in the stream-line averaged melt compositions (e.g., Nd for  $^{143}\text{Nd}/^{144}\text{Nd}$ ), respectively, for lithology  $i$ , and  $U(P)$  is the pressure-dependent rate of horizontal mantle flow normalized by the half-spreading rate. The thickness of igneous crust generated by the standard (Langmuir) and active (Brown and Lesher) RMC mixing functions is

$$H_{crust} = \frac{\sum_i^m \Phi_i^0 \int_{P_{0i}}^{P_i} F_i(P) U(P) dP}{\rho_{crust} g}. \quad (14)$$

The fundamental difference between the standard (Langmuir) and active (Brown and Lesher) RMC mixing functions is the manner in which the mantle flow function,  $U(P)$ , is quantified. For the standard (Langmuir) case, where passive flow governs, horizontal flow exiting the sides of the melting zone at any given pressure,  $u_x^{passive}(P)$ , is equivalent to the half-spreading rate,  $U_0$ . Thus,

$$U(P)_{standard} = \frac{u_x^{passive}(P)}{U_0} = 1. \quad (15)$$

For the active (Brown and Lesher) RMC case,  $U(P)$  represents a combination of the background passive flow as well as any component of active flow induced by net positive buoyancy in the source

$$U(P)_{B\&L} = \frac{u_x^{passive}(P) + u_x^{active}(P)}{U_0} = 1 + \frac{u_x^{active}(P)}{U_0}. \quad (16)$$

Below, we describe how source buoyancy is quantified and used to calculate  $u_x^{active}(P)$ .

### 3.3.2.1. Mantle Density, Source Buoyancy, and Mantle Flow in Active (Brown and Lesher) RMC Mixing Function

The net buoyancy of the source depends upon mantle temperature and the density of the individual lithologies comprising the source

$$\Delta\rho = \rho_0 \alpha^S (T_P - T_P^0) + \sum_{l=1}^k \Phi_l^0 (\rho_0 - \rho_l), \quad (17)$$

where  $\rho_0$  is the density of ambient mantle,  $T_P$  is the potential temperature of the source,  $T_P^0$  is the potential temperature of the ambient mantle,  $\Phi_l^0$  is the initial mass fraction, and  $\rho_l$  is the density of lithology  $l$ . By default, the model assumes that the ambient mantle (i.e., MORB source mantle) consists solely of peridotite. Following *Brown and Lesher* [2014], the model only considers the buoyancy of the material entering the base of the melting zone, and does not consider buoyancy changes during the melting process. If the net buoyancy of the source,  $\Delta\rho$ , entering the melting zone is zero, then mantle flow will be governed solely by passive upwelling due to plate separation (i.e.,  $u_x^{active}(P) = 0$ ). If  $\Delta\rho$  is positive, the source has excess positive buoyancy driving active upwelling, whereas if  $\Delta\rho$  is negative, the program defaults to the standard (Langmuir) RMC because the mantle is too dense to upwell.

Densities for ambient mantle and for each lithology comprising the mantle source are calculated using the CFMASN database of *Stixrude and Lithgow-Bertelloni* [2011] in the thermodynamic model *Perple\_X* [Connolly, 1990, 2005, 2009]. We have calculated densities for pyrolite [Nakagawa et al., 2012], depleted MORB mantle [Workman and Hart, 2005], harzburgite [Laporte et al., 2004], G2 pyroxenite [Pertermann and Hirschmann, 2003a,b], and MIX1G pyroxenite [Hirschmann et al., 2003; Kogiso et al., 2003] over a range of pressure (5–135 kbar) and temperature (1000–2500°C). Densities for each lithology, the bulk density of the source ( $\rho^S$ ), and the net source buoyancy are all initially calculated for the pressure-temperature conditions corresponding to the intersection of the adiabat (specified by  $T_P$ ) and the deepest solidus.

To convert net source buoyancy to mantle flow, and hence  $u_x^{active}(P)$ , REEBOX PRO first defines an “active flow volume,” which takes the shape of a cylinder [see *Brown and Lesher*, 2014, supporting information Figure S1]. The width of the cylinder is defined by the radius of buoyant upwelling,  $R$ , and the height of the cylinder is defined as the distance between the base of the crust/lithosphere and the base of the buoyant flow layer ( $H_{flow}$ ). The radius of buoyant upwelling is defined by

$$R = \left( \frac{8B\eta}{\pi g \Delta \rho^2} \right)^{(1/4)}, \quad (18)$$

and the depth to the base of the buoyant flow layer,  $H_{flow}$ , is

$$H_{flow} = \left( \frac{Q}{\frac{\Delta \rho g}{48\eta}} \right)^{(1/4)}. \quad (19)$$

In equations (18) and (19),  $B$  is the buoyancy flux,  $\eta$  is the source viscosity, and  $Q$  is the volume flux (where  $Q = \frac{B}{\Delta \rho}$ ). In *Brown and Leshar* [2014],  $\Delta \rho$  was calculated at the deepest solidus only. However, because we are most interested in constraining flow through the entire buoyant flow layer (instead of just the melting zone), REEBOX PRO recalculates lithologic densities and net source buoyancy at the base of the buoyant flow layer (assuming that the base of this layer is deeper than the deepest solidus). Thus the initial net source buoyancy calculated at the deepest solidus may differ from the net source buoyancy output by the model.

The viscosity in equations (18) and (19) is

$$\eta = \eta_0 \exp \left( \frac{E_{act} + P_{base} V_{act}}{R_{ideal} T_{base}^{real}} - \frac{E_{act} + P_{ref} V_{act}}{R_{ideal} T_{ref}^{real}} \right), \quad (20)$$

where  $\eta_0$  is reference viscosity,  $E_{act}$  is activation energy,  $V_{act}$  is activation volume,  $R_{ideal}$  is the ideal gas constant,  $T_{base}^{real}$  is the mean absolute temperature at the base of the melting zone for the specified potential temperature,  $P_{base}$  is the pressure at the base of the melting zone, and  $T_{ref}^{real}$  and  $P_{ref}$  are reference ambient conditions at the base of the melting zone [Ito et al., 1999]. The buoyancy flux,  $B$ , is related to the density contrast of the source by the empirical relationship [Brown and Leshar, 2014]

$$B = 0.89 \Delta \rho^{2.74}. \quad (21)$$

The mean flow of material into the bottom of the active flow volume ( $\overline{u_z}^{active}$ ) can be calculated assuming Poiseuille (pipe) flow [Bourdon et al., 1998]

$$\overline{u_z}^{active} = \sqrt{\frac{Bg}{8\pi\eta}}, \quad (22)$$

and is directly related to the mean flow of material out of the sides of the volume ( $\overline{u_x}^{active}$ ) by mass balance

$$\overline{u_x}^{active} = \frac{R \overline{u_z}^{active}}{2H_{flow}}, \quad (23)$$

where  $R$  is the radius of buoyant upwelling given by equation (18). The pressure-dependent form of horizontal active flow described by thin-layer theory [Ito and Mahoney, 2005; Brown and Leshar, 2014] is

$$u_x^{active}(P) = \frac{3\overline{u_x}^{active}}{2} \left[ \left( \frac{2P}{P_{flow}} \right) - \left( \frac{P}{P_{flow}} \right)^2 \right], \quad (24)$$

where  $P_{flow}$  is the pressure at the base of  $H_{flow}$

$$P_{flow} = \rho^S g H_{flow}. \quad (25)$$

The effects of this active horizontal flow on the shape of the residual mantle column/cylinder are shown in Figure 1c.

### 3.3.2.2. Bounds of Integration

The final consideration is the bounds of integration in equations (12) through (14). The upper bound,  $P_f$ , denotes the final pressure of melting, which is the pressure at the base of the newly generated igneous crust plus any preexisting lithosphere (e.g., continental lithosphere during continental breakup)

$$P_f = P_{crust} + P_{lithosphere}^{pre-existing}. \quad (26)$$

The pressure at the base of the igneous crust,  $P_{crust}$  is simply the numerator in equation (14), whereas the pressure at the base of the preexisting lithosphere,  $P_{lithosphere}^{pre-existing}$ , is assumed to be

$$P_{lithosphere}^{pre-existing} = [f_{crust} H_{lithosphere} \rho_{CC} + (1 - f_{crust}) H_{lithosphere} \rho_{LM}] g, \quad (27)$$

where  $f_{crust}$  is the crustal fraction of the lithosphere,  $\rho_{CC}$  is the density of continental crust,  $\rho_{LM}$  is the density of the lithospheric mantle, and  $H_{lithosphere}$  is the user-specified thickness of the preexisting lithosphere. The final pressure of melting,  $P_f$ , is determined by iteration because  $P_{crust}$  in equation (26) also depends upon  $P_f$  (see numerator of equation (14)).

For calculations made using the standard (Langmuir) RMC, the lower bound of integration in equations (12) through (14),  $P_{0,i}$ , defines the pressure at which the solidus of lithology  $i$  is intersected (that is, this lower bound defines the onset of melting of lithology  $i$ ; Figure 1a). For the active (Brown and Leshner) RMC, however, this bound can be either the onset of melting of lithology  $i$  (as with the standard (Langmuir) RMC), or the pressure at the base of the horizontal flow layer ( $P_{flow}$ ), whichever is shallower (Figure 1c). As noted by Ito and Mahoney [2005], this arises because buoyancy-driven flow may push upwelling, partially molten material to shallower levels within the melting zone, resulting in a residual mantle column that is shorter in length than the length of the melting zone (defined by the distance between the solidus and the base of crust  $\pm$  preexisting lithosphere).

### 3.4. Comparison of Mean Crustal Properties Derived From Different Mixing Functions

Given the importance of the mixing function in quantifying the mean properties of the igneous crust, we now highlight some of the fundamental differences between the calculated mean crustal properties derived from

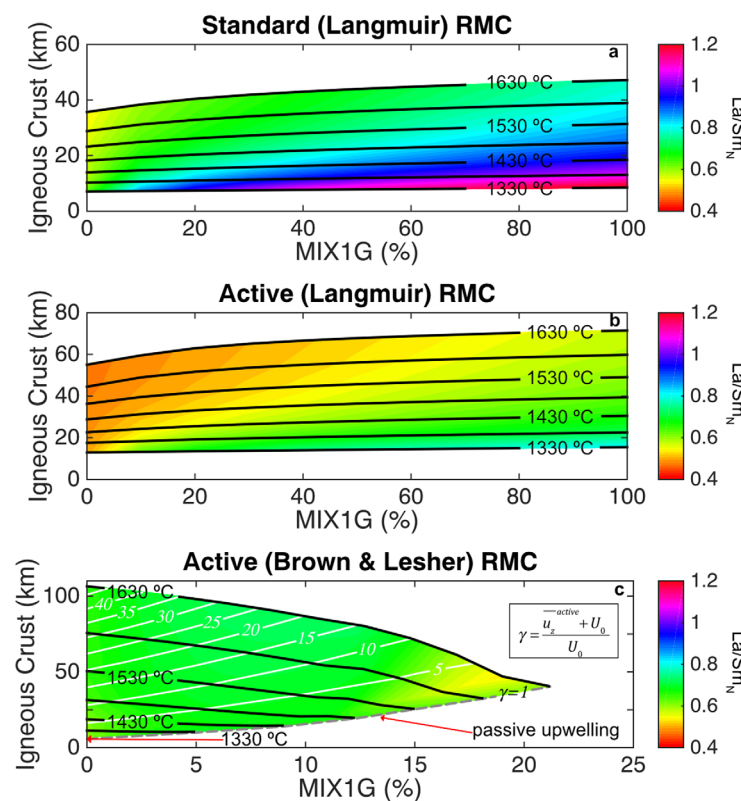


**Figure 4.** Modeled igneous crustal thickness as a function of percentage MIX1G pyroxenite in the source calculated using the (a) standard (Langmuir) RMC, (b) active (Langmuir) RMC, and (c) active (Brown and Leshner) RMC. In all plots, black contours are constant potential temperature, and the colors are contours of the chondrite-normalized [Sun and McDonough, 1989] La/Sm ratio of the bulk igneous crust. Note that the crustal thickness axes have different scales in each plot, and the proportion of MIX1G pyroxenite is limited to less than 25% in Figure 4c due to constraints from net source buoyancy. For the (c) active (Brown and Leshner) RMC, white and grey-dashed contours denote the mean upwelling velocity (passive + active) normalized by the half-spreading rate ( $\gamma$ ). The active (Brown and Leshner) RMC calculations assume ambient mantle potential temperature ( $T_0^m$ ) is 1330°C, and a half-spreading rate ( $U_0$ ) of 1.5 cm/yr. The initial mantle source composition in all calculations is depleted MORB mantle [Workman and Hart, 2005] for pyrolite peridotite and NMORB [Sun and McDonough, 1989] for MIX1G pyroxenite.

each mixing function, assuming the same initial model conditions. To facilitate comparison of the different mixing functions employed in REEBOX PRO, we used the same  $T_p$  (1330–1630°C). For the standard (Langmuir) and active (Langmuir) RMC calculations, the pyroxenite abundance varies between 0 and 100% for all  $T_p$ . For the active (Brown and Leshner) RMC calculations, the maximum pyroxenite abundances vary between 0% and the maximum amount that can be entrained at the specified  $T_p$  and still maintain at least neutral net source buoyancy. For illustrative purposes, we only ran models for sources consisting of anhydrous peridotite (pyrolite) and MIX1G pyroxenite.

Figure 4 shows crustal thickness as a function of pyroxenite abundance for all three model RMC's contoured for potential temperature and La/Sm<sub>N</sub> ratio of the bulk igneous crust. For a given potential temperature, crustal thicknesses derived from the active (Langmuir) RMC model are higher than those

for the standard (Langmuir) RMC model due to more rapid processing of mantle through the melting zone. This is also the case for the active (Brown and Lesher) RMC model that ties upwelling rate directly to source buoyancy. For peridotite-dominated sources in the active (Brown and Lesher) RMC mixing function, this buoyancy effect leads to higher mean upwelling rates (as shown by the white contours in Figure 4c) and thus enhanced overall productivity (thicker crust). However, for any given potential temperature, increasing pyroxenite content causes a decrease in the net source buoyancy, which results in decreasing mean upwelling rates and diminishing melt productivity. By  $\sim 20\%$  source pyroxenite abundance, the source is negatively buoyant and thus unable to ascend for all potential temperatures considered [see also *Brown and Lesher, 2014*].

Differences in the mean REE abundance of the igneous crust produced by the various RMC models can also be appreciated in Figure 4. For example, the standard (Langmuir) RMC exhibits the greatest range ( $\text{La}/\text{Sm}_N \sim 0.53\text{--}1.20$ ), whereas the active (Langmuir) and active (Brown and Lesher) RMC are generally lower and more uniform ( $\text{La}/\text{Sm}_N \sim 0.47\text{--}0.80$ , and  $\sim 0.53\text{--}0.72$ , respectively). Nevertheless, the standard (Langmuir) and active (Langmuir) RMC show similar  $\text{La}/\text{Sm}_N$  systematics. For example, at any given pyroxenite abundance,  $\text{La}/\text{Sm}_N$  decreases with increasing potential temperature due to the higher extents of melting at higher temperatures. Likewise, for any given potential temperature, both mixing functions show an increase in  $\text{La}/\text{Sm}_N$  as pyroxenite content increases due to the higher initial  $\text{La}/\text{Sm}_N$  composition of the pyroxenite source. However, for any given potential temperature and pyroxenite abundance, the active (Langmuir) RMC has lower  $\text{La}/\text{Sm}_N$  compared to the standard (Langmuir) RMC because of the higher extents of melting in the active (Langmuir) RMC (compare equations (9) and (12)).

In contrast, the  $\text{La}/\text{Sm}_N$  systematics observed in the standard (Langmuir) and active (Langmuir) RMC are less obvious in the active (Brown and Lesher) RMC, which exhibits a much more restricted range of  $\text{La}/\text{Sm}_N$  because of the different weighting of melts due to the active flow (compare RMC in Figure 1). Nevertheless, of the three mixing functions,  $\text{La}/\text{Sm}_N$  for the active (Brown and Lesher) RMC model is the highest for a given potential temperature and pyroxenite content because this mixing function favors low degree melts derived deeper in the melting zone more heavily than the standard (Langmuir) or active (Langmuir) RMC (as governed by equations (16) and (24); compare also the shapes of the residual mantle columns in Figure 1). These differences can be expected for any ratio of incompatible trace elements where the element in the numerator is more incompatible than in the denominator.

## 4. Applications

REEBOX PRO is designed to model mantle melting over a wide range of conditions applicable to divergent margin environments (e.g., variable  $T_p$  and  $T_p^0$ , a variety of source lithologies having different trace element and isotopic compositions, different styles of mantle flow, and the effects of preexisting lithospheric lids). In our previous work [*Brown and Lesher, 2014*], we demonstrated its utility for simulating (1) melt generation on a regional scale, (2) melting beneath a continent during continental breakup (incorporating a preexisting lithospheric lid), (3) melting along a mid-ocean ridge, and (4) the effects of thermal insulation beneath supercontinents on melting (using variable  $T_p^0$ ). Here, we highlight new functionality, including melting involving hydrous and depleted peridotite. We also illustrate how REEBOX PRO model outputs may be used “offline” to evaluate different melt mixing/pooling scenarios, drawing on recent work by *Rudge et al.* [2013].

### 4.1. Hydrous Peridotite Melting

We benchmark our hydrous melting model against the results presented by *Asimow and Langmuir* [2003]. These authors noted that hydrous melting can result in fundamental differences in the relationships between basalt composition and volume compared to anhydrous melting. For anhydrous melting of mantle upwelling passively through a 2-D melting zone, the general expectation is that igneous crustal thickness ( $H_{crust}$ ) increases as the mean extent of melting ( $F_B$ ) increases (i.e., more melting produces thicker crust), where  $F_B$  (mean extent of melting) is defined as the mass of melt generated in the melting zone divided by the mass flux of solid mantle entering the base of the melting zone. However, the addition of water to the mantle source can lead to a negative correlation between  $H_{crust}$  and  $F_B$  under the same mantle flow conditions. This results from the low melt productivity of hydrous melting below the anhydrous solidus (see Figure 2), which lowers  $F_B$  compared to an anhydrous source melting under the same conditions. Furthermore,

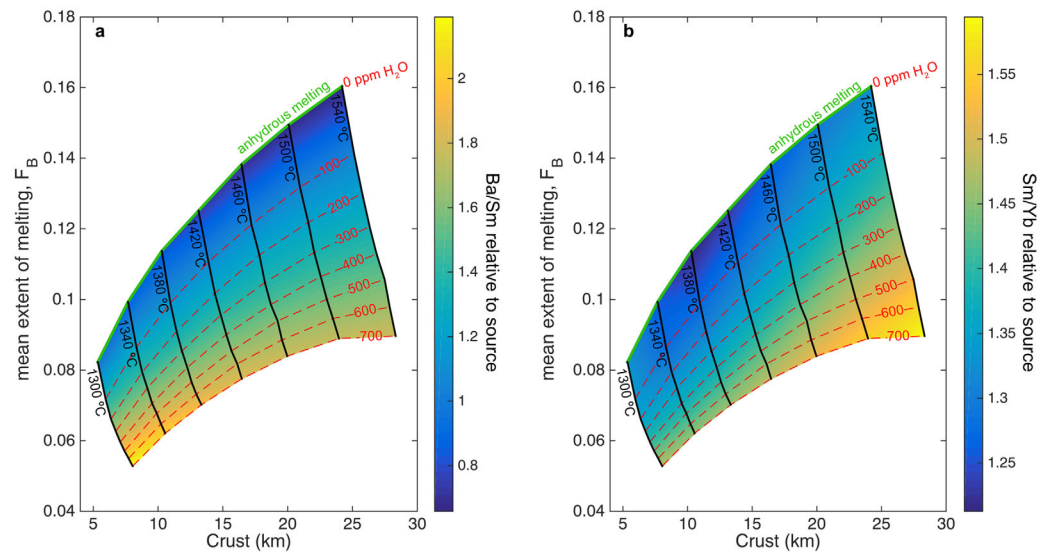


**Figure 5.** Igneous crustal thickness versus mean extent of melting ( $F_B$ ) as a function of mantle potential temperature (black contours) for a (pyrolyte) peridotite source containing 0–700 ppm water (red-dashed contours). Green curve represents anhydrous melting. (a) Colors represent relative enrichment of Ba/Sm in bulk igneous crust relative to the source. Lower mean extents of melting due to increasing water contents result in stronger enrichments in Ba relative to Sm. (b) Colors represent relative enrichment of Sm/Yb in bulk igneous crust relative to the source. Increasing water contents and mantle potential temperatures result in melting within the garnet stability field, which results in a fractionation of Yb (more compatible in garnet) from Sm (less compatible in garnet). Initial mantle source composition in all calculations is depleted MORB mantle [Workman and Hart, 2005]. All calculations made using standard (Langmuir) RMC. After Asimow and Langmuir [2003].

as noted by Asimow and Langmuir [2003], the lower mean  $F$  associated with hydrous melting results in enrichment of incompatible trace element concentrations relative to anhydrous melting (since the enrichment in the melt relative to the source for a perfectly incompatible trace element is  $1/F_B$ ). Finally, for mid-ocean ridge spreading systems, peridotite melting models indicate that average oceanic crustal thicknesses are generated for mantle potential temperatures that intersect the peridotite solidus within the spinel stability field [e.g., Klein and Langmuir, 1987; McKenzie and Bickle, 1988; Langmuir et al., 1992]. However, for water-bearing peridotite, the onset of melting can be deeper where garnet is stable and thus deep hydrous melting may produce initial melts strongly depleted in heavy rare earth elements (relative to the middle rare earth elements).

To assess whether the peridotite melting functions incorporated into REEBOX PRO capture these features of hydrous melting, we ran the model for a range of  $T_P$  (1300–1540°C) and source water contents (0–700 ppm) assuming passive upwelling (standard (Langmuir) RMC) of a homogeneous peridotite source. Using model outputs of melt fraction ( $F$ ) and pressure ( $P$ ), we calculated the mean extent of melting as [Asimow et al., 2001]

$$F_B = \frac{\int_{P_0}^{P_f} F dP}{P_f - P_0}. \quad (28)$$

Figure 5 shows the expected positive correlation between  $F_B$  and  $H_{crust}$  for anhydrous melting and negative correlation for hydrous melting (compare with Figure 2 of Asimow and Langmuir [2003]). For any given  $T_P$ , REEBOX PRO further predicts strong enrichments of highly incompatible trace elements in pooled melts, shown for Ba/Sm in Figure 5a, and strong depletions in elements compatible in garnet i.e., higher Sm/Yb (Figure 5b) with increasing  $H_2O$  content of the source. Both results are consistent with the model predictions of Asimow and Langmuir [2003]. In terms of overall melt productivity, REEBOX PRO further predicts that regardless of  $T_P$ , increasing the source water content to 700 ppm  $H_2O$  only results in an additional 4 km in crustal thickness (Figure 5). While this increase in crustal thickness is significant, such “wet” mantle melting under ambient mantle conditions cannot account for the anomalously thick igneous crust found at, for example, Iceland [e.g., Brown and Lesher, 2014].

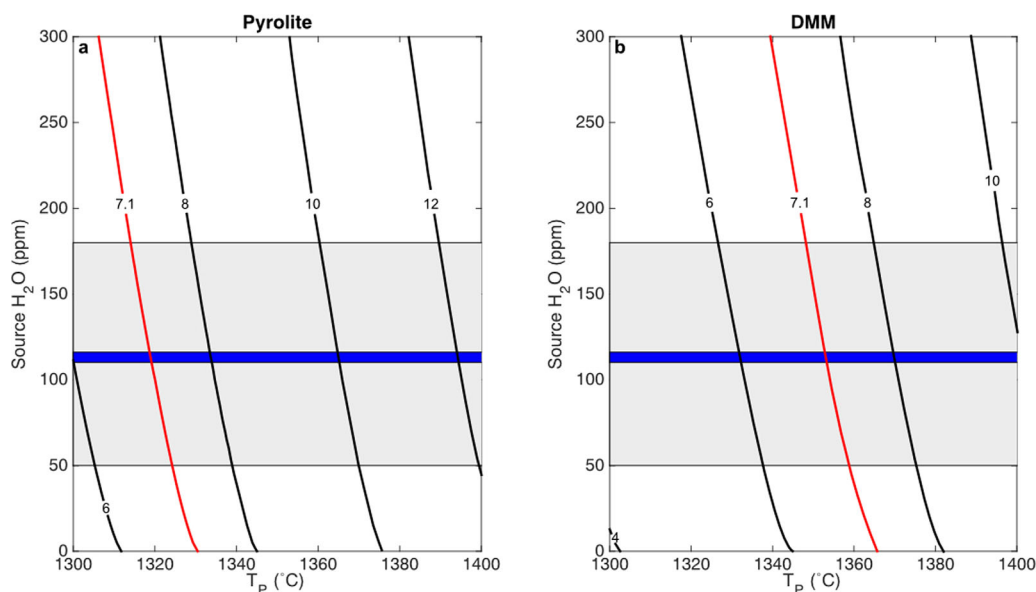


**Figure 6.** Quantifying ambient mantle potential temperature,  $T_p^0$ , using (a) fertile (pyrolite), and (b) depleted (DMM) peridotite sources. Black contours are model igneous crustal thickness (km), and red contours are average oceanic crustal thickness of 7.1 km. The grey field represents the range of estimated water contents for the global spreading ridge system (50–180 ppm) [Salters and Stracke [2004]; Workman and Hart [2005]]. The blue band represents best estimates of water content for the depleted MORB mantle source (110–116 ppm) [Salters and Stracke, 2004; Workman and Hart, 2005]. Depleted peridotite requires higher ambient potential temperatures than fertile peridotite to generate the average oceanic crustal thickness. All calculations made using the standard (Langmuir) RMC.

#### 4.2. Ambient Mantle Potential Temperature and Pooled Melt Composition

An instructive test for REEBOX PRO is to quantify the potential temperature of the mantle needed to yield average oceanic crust that is  $7.1 \pm 1$  km thick [White *et al.*, 1992]. A common modeling method for quantifying  $T_p^0$  is to assume adiabatic decompression melting of a homogeneous, anhydrous peridotite source, and complete pooling of all melts generated within a 2-D passive upwelling, corner-flow melting regime [e.g., Spiegelman and McKenzie, 1987; McKenzie and Bickle, 1988; Bown and White, 1994; Iwamori *et al.*, 1995]. We follow this general approach here, but expand our analysis in two key ways. First, we determine  $T_p^0$  for fertile and depleted anhydrous peridotite sources that yields the average oceanic crustal thickness. Then we consider the effects of  $H_2O$  on estimates of  $T_p^0$  assuming the MORB source contains on average  $\sim 113$  ppm  $H_2O$  [Salters and Stracke, 2004; Workman and Hart, 2005].

The results are shown in Figure 6a for a pyrolitic source and Figure 6b for depleted lherzolite (DMM). Not surprisingly, melting pyrolite requires lower  $T_p$  than melting of depleted lherzolite to produce the target crustal thickness, while varying the water content is not found to change this relationship (see Figure 6a). For example, for anhydrous pyrolite, 7.1 km thick crust can be generated for a  $T_p$  of 1330°C, while if the source contains 300 ppm  $H_2O$   $T_p$  is 1306°C. Similarly, for depleted lherzolite (Figure 6b) average oceanic crust can be formed under anhydrous conditions for a  $T_p$  of 1366°C, while adding 300 ppm  $H_2O$  to the source reduces  $T_p$  to 1340°C. Finally, if the MORB source contains 110–116 ppm  $H_2O$  as proposed by Salters and Stracke [2004] and Workman and Hart [2005], then a potential temperature of 1319°C would yield average oceanic crustal thickness from pyrolitic mantle, but would require  $T_p = 1353^\circ\text{C}$  if the source was depleted lherzolite. These differences in  $T_p^0$  (1319–1366°C) are not great and are well within the estimates of others (1315–1454°C) [Kinzler and Grove, 1992b; Asimow *et al.*, 2001; Herzberg *et al.*, 2007; Putirka *et al.*, 2007; Lee *et al.*, 2009; Putirka, 2016]. What this modeling does illustrate is that modest variations in lherzolite composition and water content of the mantle source do not have substantial effects on ambient mantle potential temperature estimates.

Given the range in estimated  $T_p^0$  for the hydrous/anhydrous fertile (1319/1330°C, respectively) and depleted (1353/1366°C, respectively) peridotite sources, we now explore what effect, if any, the choice of hydrous or anhydrous fertile or depleted peridotite (and the associated range of  $T_p^0$ ) has on modeled primary MORB compositions. To do this, we modeled the fertile and depleted peridotite sources using either 0 or 113 ppm

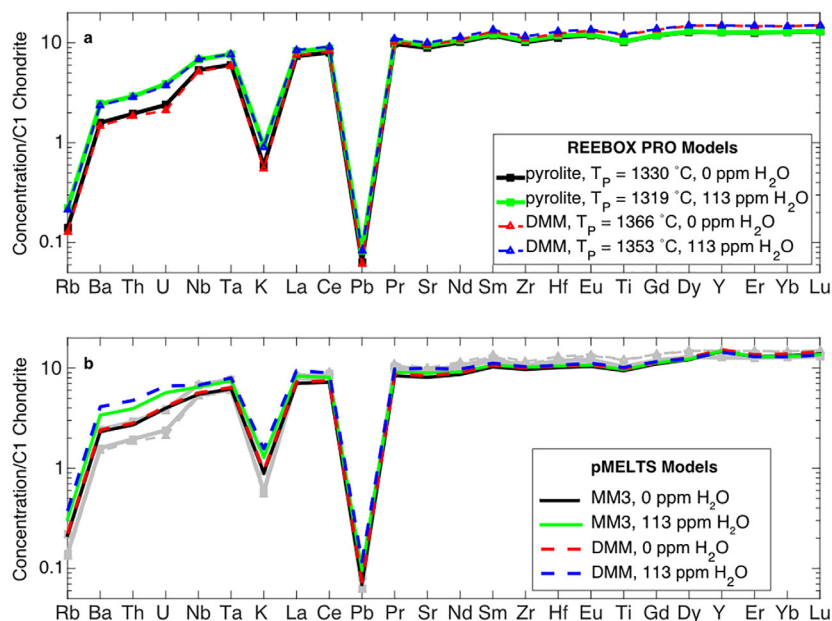


**Figure 7.** Chondrite-normalized [Sun and McDonough, 1989] modeled pooled melt compositions calculated using the standard (Langmuir) mixing function and an initial trace element composition of depleted MORB mantle from Workman and Hart [2005]. (a) Results from REEBOX PRO using “dry” (0 ppm  $\text{H}_2\text{O}$ ) and “wet” (113 ppm  $\text{H}_2\text{O}$ ) fertile (pyrolite) and depleted (DMM) peridotite. (b) Same as Figure 7a, with REEBOX PRO results from Figure 7a in gray and the addition of pooled melt compositions calculated using pMELTS [Ghiorso *et al.*, 2002] and alphaMELTS [Smith and Asimow, 2005] assuming “dry” (0 ppm  $\text{H}_2\text{O}$ ) and “wet” (113 ppm  $\text{H}_2\text{O}$ ) MM3 (fertile) [Baker and Stolper [1994] and DMM (depleted) [Workman and Hart [2005] peridotite. The bulk igneous crustal thickness in all REEBOX PRO and pMELTS models is between 7.06 and 7.18 km.

$\text{H}_2\text{O}$  (113 ppm  $\text{H}_2\text{O}$  is the average value of the best estimates for DMM of Salters and Stracke [2004] and Workman and Hart [2005]), assuming the peridotite source has an initial trace element composition of DMM [Workman and Hart, 2005]. Figure 7 shows the results for modeled pooled melt compositions as a function of the different source conditions.

As can be seen in Figure 7a, for the same  $\text{H}_2\text{O}$  content (i.e., 0 or 113 ppm  $\text{H}_2\text{O}$ ), the fertile and depleted peridotite compositions in REEBOX PRO generate pooled melt compositions that are virtually indistinguishable from each other. However, when comparing hydrous and anhydrous pooled melt compositions for a given peridotite source (i.e., fertile or depleted), the anhydrous compositions differ from the hydrous compositions. In particular, the abundances of the very incompatible elements (Rb-K) are more elevated in the hydrous pooled melt compositions than the anhydrous pooled melts, whereas the moderately incompatible elements (La-Lu) are nearly identical. The enrichment of the very incompatible elements in the hydrous pooled melts is simply a consequence of the lower mean extent of melting in the hydrous source compared to the anhydrous source (see discussion above). These results are consistent with the trace element compositions of pooled melt compositions derived using pMELTS [Ghiorso *et al.*, 2002] (pooled melt compositions were calculated with the alphaMELTS package of Smith and Asimow [2005]; Figure 7b). From these results, it is apparent that from a melt trace element composition perspective, the choice of depleted or fertile peridotite is significantly less important than whether or not the peridotite source contains  $\text{H}_2\text{O}$ .

#### 4.3. Additional Melt Mixing/Pooling Possibilities

In this final section, we provide an example of how REEBOX PRO outputs can be used for calculating melt-melt mixing “off-line”. For example, one may use REEBOX PRO outputs to calculate the statistical distribution of melt compositions derived from random mixing of instantaneous melts generated within a lithologically heterogeneous mantle source using the method presented by Rudge *et al.* [2013]. Assuming a basalt composition represents a weighted average of instantaneous melts, this method employs the Dirichlet probability distribution to randomly weight the contributions of the instantaneous melts to the model basalt composition. Using the nomenclature from Rudge *et al.* [2013], the model basalt composition (i.e., mixture of instantaneous melts) can be quantified as

$$\hat{C} = \sum_{j=1}^m \sum_{i=1}^{n_j} \hat{r}_j^i c_j^i. \tag{29}$$

Here,  $m$  is the number of source lithologies generating melt,  $n_j$  is the number of instantaneous melt “packages” generated during melting of lithology  $j$  (for the modeling presented here, this is the number of decompression steps),  $c_j^i$  is the instantaneous melt composition of melt package  $i$  derived from lithology  $j$  (a REEBOX PRO model output), and  $\hat{r}_j^i$  is a random weighting factor that determines how each instantaneous melt package  $i$  derived from lithology  $j$  contributes to the model basalt composition.

The random weighting factors,  $\hat{r}_j^i$ , are subject to a number of constraints, including that they must be positive values, must sum to unity (i.e., mass balance), and must generate model basalt compositions that reproduce the mean bulk crust melt composition as determined by the specified mixing function [Rudge *et al.*, 2013]. The random weights from the Dirichlet distribution are

$$\{\hat{r}_1^1, \dots, \hat{r}_1^{n_1}, \dots, \hat{r}_m^1, \dots, \hat{r}_m^{n_m}\} \sim \text{Dir}(\alpha_1^1, \dots, \alpha_1^{n_1}, \dots, \alpha_m^1, \dots, \alpha_m^{n_m}), \tag{30}$$

where

$$\alpha_j^i = (N-1) f_j \tilde{\omega}_j^i. \tag{31}$$

In equation (31),  $N$  is the “mixing factor,” which ranges from 1 to  $\infty$ , and determines the degree to which the instantaneous melts are mixed together (increasing  $N$  results in more mixing, with complete mixing given by  $N = \infty$ ). The  $f_j \tilde{\omega}_j^i$  term ensures that the random weighting reproduces the bulk crust composition [Rudge *et al.*, 2013]. Here,  $f_j$  is the proportion of melt derived from lithology  $j$  in the bulk crust, and  $\tilde{\omega}_j^i$  is a weighting function that relates the instantaneous melt compositions from lithology  $j$  to the mean pooled melt composition for that lithology (see equation (2) in Rudge *et al.* [2013]). The weighting function depends on the mixing function used to calculate the bulk crust composition, where for the standard (Langmuir) RMC mixing function

$$\tilde{\omega}_j^i = \frac{(P^i - P_f) \left(\frac{dF_j^i}{dP}\right)}{\sum_{i=1}^{n_j} (P^i - P_f) \left(\frac{dF_j^i}{dP}\right)}; \tag{32}$$

for the active (Langmuir) RMC mixing function

$$\tilde{\omega}_j^i = \frac{\left(\frac{dF_j^i}{dP}\right)}{\sum_{i=1}^{n_j} \left(\frac{dF_j^i}{dP}\right)}; \tag{33}$$

and for the active (Brown and Lesher) RMC mixing function

$$\tilde{\omega}_j^i = \frac{(P^i - P_f) U^i \left(\frac{dF_j^i}{dP}\right)}{\sum_{i=1}^{n_j} (P^i - P_f) U^i \left(\frac{dF_j^i}{dP}\right)}. \tag{34}$$

In these equations  $P^i - P_f$  is the pressure below the top of the melting zone, and  $\left(\frac{dF_j^i}{dP}\right)$ , and  $U^i$  are the polybaric productivity of lithology  $j$  and the normalized horizontal velocity out of the melting zone (constrained by equations (16) and (24)), respectively, during decompression step  $i$ .

Figure 8 shows model basalt compositions calculated by equation (29) using the standard (Langmuir) RMC mixing function for a source containing 90% anhydrous pyrolite peridotite and 10% G2 pyroxenite, and  $T_p = 1450^\circ\text{C}$ . Low mixing factors result in a much wider spectrum of compositions, with the limit of  $N = 1$  resulting in the instantaneous melt compositions derived from each lithology. In contrast, increasing the mixing factor results in a clustering of model basalt compositions around the bulk crust average calculated using REEBOX PRO (red square). Importantly, linear correlations between La/Nd and  $^{143}\text{Nd}/^{144}\text{Nd}$  are not observed with increasing  $N$ , which is in agreement with the results of Rudge *et al.* [2013], who used pMELTS and a different pyroxenite bulk composition in their calculations.

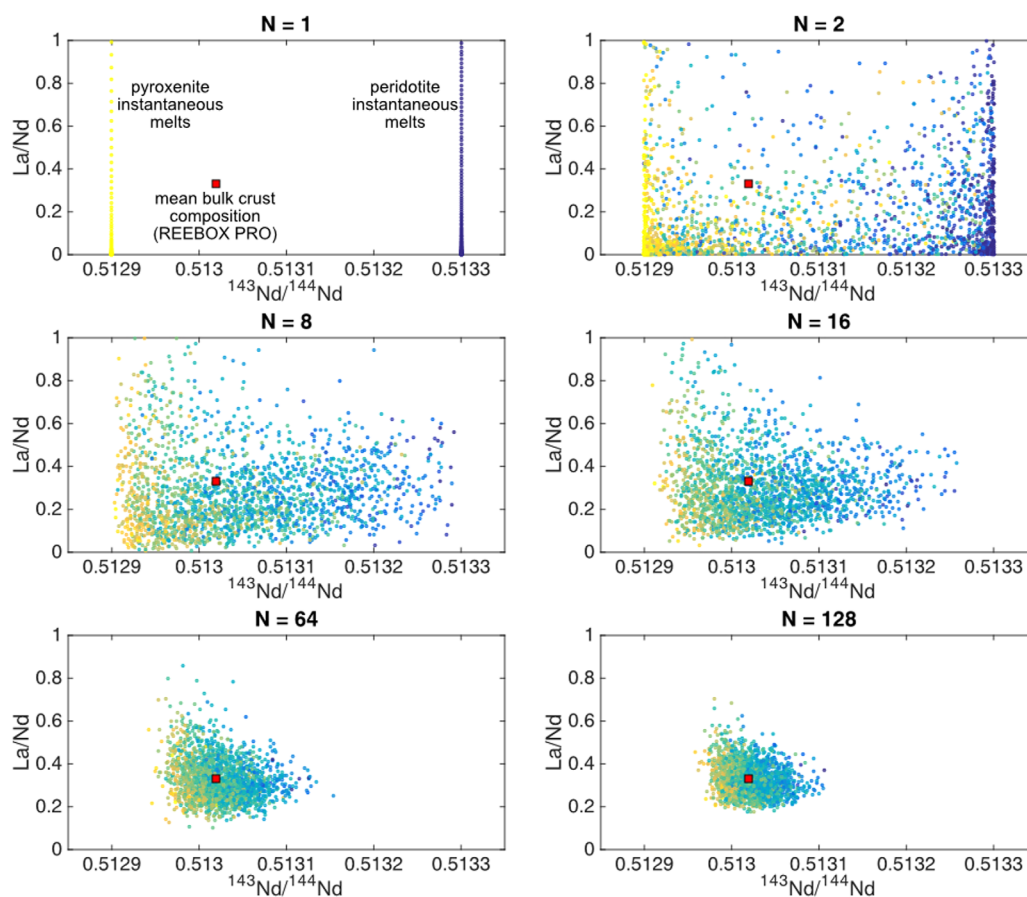


**Figure 8.** Model results (La/Nd versus  $^{143}\text{Nd}/^{144}\text{Nd}$ ) for basalt compositions calculated for a source consisting of 90% anhydrous pyroxenite/10% G2 pyroxenite using Dirichlet-distributed random weights for all instantaneous melt compositions. Each plot depicts results for a different mixing factor (higher mixing factors indicate more complete mixing). Symbol colors denote proportion of pyroxenite melt in the mixture, with 100% peridotite in dark blue, and 100% pyroxenite in bright yellow. The red squares mark the mean bulk crust composition calculated using REEBOX PRO using the standard (Langmuir) RMC mixing function. The peridotite source has an initial trace element composition of DMM [Workman and Hart, 2005], with  $^{143}\text{Nd}/^{144}\text{Nd} = 0.5133$ . The pyroxenite source has an initial trace element composition of NMORB [Sun and McDonough, 1989], with  $^{143}\text{Nd}/^{144}\text{Nd} = 0.5129$ . Increasing mixing factors result in a clustering of model basalt compositions around the mean bulk crust composition. Each plot shows 2000 model basalt compositions.

Equation (29) may also be used to calculate model basalt compositions in which all instantaneous melts below a specified depth are uniformly pooled and randomly mixed with instantaneous melts generated at shallower levels in the melting zone. Figure 9 shows such a case, where all instantaneous pyroxenite and peridotite melts generated below 2.75 GPa have been homogenized (pooled) together to form a single composition (termed “deep homogenized peridotite + pyroxenite melts” in Figure 9) that is then randomly mixed with the pyroxenite and peridotite instantaneous melts generated above 2.75 GPa. Unlike the previous mixing example (Figure 8), this scenario generates linear correlations between La/Nd and  $^{143}\text{Nd}/^{144}\text{Nd}$  with increasing mixing factor, which is also in agreement with Rudge *et al.* [2013]. Thus, REEBOX PRO can be used to calculate not only bulk crust compositions (standard model output), but also enables one to evaluate, offline, basalt compositions generated by different methods for mixing instantaneous melts within the melting zone, as illustrated here.

## 5. Summary

Here, we have presented the theoretical and mathematical underpinnings of the forward mantle melting model REEBOX PRO, which can simulate melt generation in lithologically homogeneous and heterogeneous mantle sources. Written as a stand-alone executable program, REEBOX PRO simulates adiabatic decompression melting and calculates melt compositions using thermodynamic and experimental constraints on the

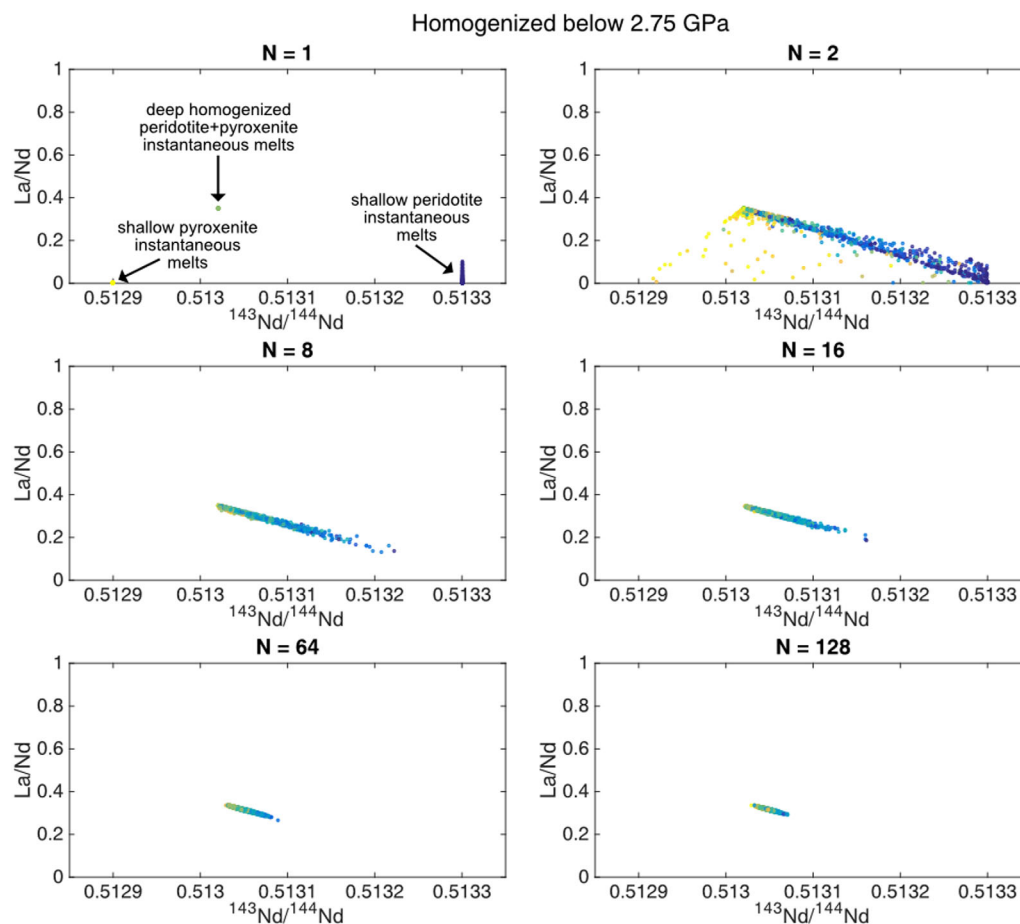


**Figure 9.** Model results (La/Nd versus  $^{143}\text{Nd}/^{144}\text{Nd}$ ) for basalt compositions calculated for the same source conditions as in Figure 8 using Dirichlet-distributed random weights for all instantaneous melt compositions. For these models, all melts below 2.75 GPa have been homogenized together to form a single composition that mixes with instantaneous peridotite and instantaneous pyroxenite melts generated higher in the melting zone (see top left panel). Each plot depicts results for a different mixing factor (higher mixing factors denote more complete mixing). Symbol colors are the same as in Figure 8. Linear correlations between La/Nd and  $^{143}\text{Nd}/^{144}\text{Nd}$  result with increasing mixing factor. Each plot shows 2000 model basalt compositions.

melting behaviors and mineral-melt partitioning behavior of anhydrous peridotite, hydrous peridotite, harzburgite, silica saturated and undersaturated pyroxenite. The program offers three different melt pooling scenarios: a triangular corner flow melting zone governed by passive upwelling (standard (Langmuir) RMC mixing function); an active upwelling melting zone induced by buoyancy changes during melting, where all melting columns decompress to the base of the crust/lithosphere (active (Langmuir) RMC mixing function); and an active upwelling melting zone induced by intrinsic density contrasts between the model mantle source and ambient mantle, where flow out of the sides of a triangular melting zone increases with depth (active (Brown and Lesher) RMC mixing function). REEBOX PRO takes user inputs for mantle potential temperature, initial lithologic abundance(s), initial trace element and Sr, Nd, Hf, and Pb isotopic compositions for the specified lithologies, thickness of any preexisting continental lithosphere, half-spreading rate, and ambient mantle potential temperature, and outputs the calculated trace element and isotopic composition of the bulk igneous crust (for the specified mixing function), as well as all instantaneous melt compositions, all column-accumulated melt compositions, and all pooled melt compositions.

We have shown how the different mixing functions produce different bulk crust compositions and crustal thicknesses. Crustal thicknesses calculated using either of the active upwelling mixing functions (active (Langmuir) or active (Brown and Lesher) RMC) are thicker than the standard (Langmuir) RMC because more melt is processed through the melting zone with the former mixing functions. Pooled melt compositions for the active upwelling mixing functions are more restricted than those predicted using the standard RMC. Most notably,

the active (Brown and Lesher) RMC mixing function predicts higher mean values for incompatible trace element ratios where the numerator element is more incompatible than the denominator element because this mixing function weights low degree melts in the final pooled melt more heavily than the other mixing functions.

To benchmark the program, and highlight some of its functionality, we have used REEBBOX PRO to simulate hydrous peridotite melting beneath mid-ocean ridges and have shown that the model results are consistent with the predictions and modeling results of *Asimow and Langmuir* [2003]. We have also used REEBBOX PRO to constrain ambient mantle temperatures and to model primary MORB trace element compositions. We showed that our modeled ambient mantle potential temperatures are consistent with other independent estimates and that primary MORB trace element compositions are more sensitive to source water contents than the relative depletion of the peridotite source. Finally, we showed that results from REEBBOX PRO can be applied to “off-line” mixing calculations by reproducing the general mixing systematics predicted for random mixing of instantaneous melts from a lithologically heterogeneous source, as presented by *Rudge et al.* [2013]. These benchmarks and modeling examples, combined with our previous application of the model to North Atlantic magmatism [*Brown and Lesher, 2014*], demonstrate that REEBBOX PRO is sufficiently flexible to model basalt petrogenesis for a broad range of contexts.

### Appendix A: Melting Parameterizations

Application of equations (2) and (3) in the main text to quantify the melting function requires that the partial derivatives  $\frac{\partial T}{\partial F}$  and  $\frac{\partial T}{\partial P}$  be determined for each lithology as melting progresses. In REEBBOX PRO, we calculate these partial derivatives using finite difference on  $P$ - $T$ - $F$  parameterizations of high pressure melting experiments. A common parameterization technique is to derive a quantitative relationship between melt fraction,  $F$ , as a function of homologous temperature,  $T'$ ,

$$F=f(T'), \tag{A1}$$

where homologous temperature is quantified as the fractional temperature between the solidus and liquidus temperatures

$$T' = \frac{T - T_{\text{solidus}}(P)}{T_{\text{liquidus}}(P) - T_{\text{solidus}}(P)}. \tag{A2}$$

Because parameterizations of  $T'$  can be rearranged to solve for  $T$  as an explicit function of  $P$  and  $F$ , these parameterizations are used to calculate partial derivatives by finite difference.

In REEBBOX PRO, we utilize a combination of existing and newly developed  $T$ - $P$ - $F$  parameterizations for the included source lithologies to quantify the necessary partial derivatives. For example, we apply the *Katz et al.* [2003] anhydrous and hydrous peridotite melting parameterizations for lherzolite and harzburgite assemblages. For pyroxenite, we utilize the parameterization of *Pertermann and Hirschmann* [2003a,b] for the G2 bulk composition, and have developed a new  $T$ - $F$ - $P$  parameterization for the MIX1G bulk composition based upon the experimental results of *Hirschmann et al.* [2003] and *Kogiso et al.* [2003]. For the latter, we use a solidus parameterization from *Till et al.* [2010], as described below.

#### A1. Anhydrous Peridotite and Harzburgite

REEBBBOX PRO simulates melting for three types of anhydrous peridotite bulk composition-anhydrous pyrolite, anhydrous-depleted MORB mantle (DMM based on *Workman and Hart* [2005]), and harzburgite (based on the Depma harzburgite bulk composition studied by *Laporte et al.* [2004]). To simulate melting of these lithologies, we have applied modified versions of the anhydrous and hydrous peridotite melting parameterizations of *Katz et al.* [2003] because they have different solidi, and clinopyroxene modes (which are key variables in the *Katz et al.* parameterization).

The first modification is that we use our own parameterizations of clinopyroxene mineral modes and melting reactions for the pyrolite, DMM, and harzburgite (details of the mineral mode and melting reaction parameterizations are provided in Appendix B). Next, for the pyrolite bulk composition, we employ the anhydrous peridotite solidus of *Katz et al.* [2003]

$$T_{\text{solidus}}^{\text{pyrolite}} = 1085.7 + 132.9P - 5.1P^2, \tag{A3}$$

where  $P$  is in GPa.

To quantify the solidus for DMM, we applied the 1 GPa solidus temperature parameterization of *Wasylenki et al.* [2003], which is based on the concentration of Na<sub>2</sub>O, K<sub>2</sub>O, and P<sub>2</sub>O<sub>5</sub> in near-solidus melts (total melt fraction = 0.05%) calculated by pMELTS [Ghiorso *et al.*, 2002]. Using pMELTS to calculate the near-solidus melt composition of DMM [Workman and Hart, 2005] melts at 1 GPa, we applied the *Wasylenki et al.* parameterization, resulting in a modeled solidus temperature of ~1250°C for DMM at 1 GPa. This estimated solidus temperature is ~36.5°C hotter than the *Katz et al.* solidus at 1 GPa. As we lack constraints on the DMM solidus temperature at higher pressures, we therefore utilize the *Hirschmann* [2000] solidus for DMM across all *P* because it is 35°C hotter than the *Katz et al.* [2003] solidus across all *P*,

$$T_{solidus}^{depleted\_peridotite} = 1120.7 + 132.9P - 5.1P^2. \tag{A4}$$

Because existing experimental constraints on the Depma harzburgite bulk composition [Laporte *et al.*, 2004] indicate this solidus is ~61.5°C warmer than the *Katz et al.* dry peridotite solidus parameterization at 1 GPa, we model the harzburgite solidus by adding 61.5°C to the *Katz et al.* [2003] solidus across all *P*,

$$T_{solidus}^{harzburgite} = 1147.2 + 132.9P - 5.1P^2. \tag{A5}$$

Finally, given the lack of experimental constraints, we do not consider changes in bulk composition on liquidus temperature (although in theory they should be slightly different). Consequently, we apply the *Katz et al.* [2003] anhydrous melting liquidus parameterization to DMM and harzburgite, which, given the differences in solidus temperatures between these lithologies, ensures that DMM has a higher polybaric productivity than pyroxenite and harzburgite has a higher polybaric productivity than DMM, as predicted by theory [Hirschmann *et al.*, 1999] and shown by melting experiments [Wasylenki *et al.*, 2003] (see Figure 2a in the main text).

### A2. Hydrous Peridotite

We employ the hydrous melting parameterization of *Katz et al.* [2003] to simulate melting of hydrous peridotite. This parameterization quantifies the magnitude of the freezing point depression ( $\Delta T$ ) due to water, which is subtracted uniformly from the anhydrous solidus and liquidus at each *P*. From *Katz et al.* [2003], the freezing point depression as a function of mantle water content is

$$\Delta T(X_{H_2O}) = 43X_{H_2O}^{0.75}, \tag{A6}$$

where  $X_{H_2O}$  is the dissolved water fraction in the melt (given in weight fraction).  $X_{H_2O}$  is related to the bulk water content in the source by the batch melting equation [Shaw, 1970]

$$X_{H_2O} = \frac{X_{H_2O}^{bulk}}{F + D_{H_2O}(1-F)}, \tag{A7}$$

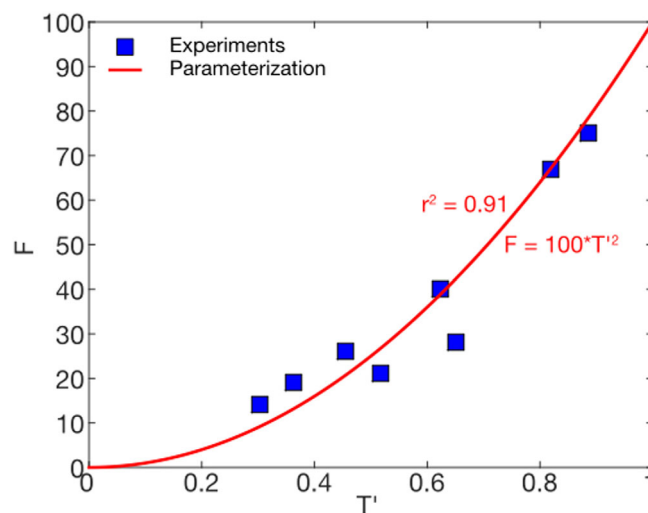


**Figure A1.** Melt fraction versus homologous temperature ( $T'$ ) for MIX1G pyroxenite. Blue squares are experimental results [Hirschmann *et al.*, 2003; Kogiso *et al.*, 2003]. Best-fit curve through experimental data is shown in red.

where  $X_{H_2O}^{bulk}$  is the initial bulk water content,  $D_{H_2O}$  is the bulk partition coefficient for water (0.008; Hirschmann, 2006), and  $F$  is the total extent of melting.

### A3. G2 Pyroxenite and MIX1G Pyroxenite

We employ the parameterization of *Petermann and Hirschmann* [2003a,b] for G2 pyroxenite melting. For MIX1G pyroxenite [Hirschmann *et al.*, 2003; Kogiso *et al.*, 2003], we have developed a new *P-T-F* parameterization. For this parameterization, we require expressions for the pressure dependence of the solidus and liquidus temperatures. We use the MIX1G solidus parameterization given by *Till et al.*

[2010], which is based on experimental results [Hirschmann *et al.*, 2003; Kogiso *et al.*, 2003]

$$T_{solidus}^{MIX1G} = 1096.8 + 120.95P - 3.4535P^2, \tag{A8}$$

with  $P$  in GPa. We also utilize the MIX1G liquidus parameterization of Lambart *et al.* [2013] based upon the same experimental results

$$T_{liquidus}^{MIX1G} = 1343 + 73.6P. \tag{A9}$$

Using these solidus and liquidus parameterizations, and assuming a quadratic form between  $F$  and  $T'$  [Lambart *et al.*, 2013], we derive a least squares best fit relationship (Figure A1) based on experimental results [Hirschmann *et al.*, 2003; Kogiso *et al.*, 2003], which results in

$$T = T_{solidus}^{MIX1G} + \sqrt{F \left( T_{liquidus}^{MIX1G} - T_{solidus}^{MIX1G} \right)^2}. \tag{A10}$$

## Appendix B: Modeling Mineral Mode and Melting Reaction Evolution During Decompression Melting

The modal abundances of the minerals comprising the residue of any given lithology change as a function of  $P$  and  $F$ . Changes in pressure govern the stability of the aluminous phases (e.g., spinel and garnet), which are governed by subsolidus mineral-mineral reactions [O'Neill, 1981; Robinson and Wood, 1998; Klemme and O'Neill, 2000; Walter *et al.*, 2002; Klemme, 2004]. Changes in mineral mode due to melt depletion are governed by the melting reaction stoichiometry.

To quantify these effects due to pressure and melting, we first parameterized the available experimental data for fertile peridotite. We then extended the fertile peridotite parameterization to more depleted peridotite compositions, including depleted MORB mantle and harzburgite. It should be noted that because these parameterizations are based on batch melting experiments, they provide only an approximation for modeling (near) fractional mineral mode evolution. Nevertheless, they provide a starting point for such modeling and can easily be modified as new experimental constraints become available.

In general, we separate the effects of melt depletion from the effects of pressure by first parameterizing the modes of all stable phases along the solidus, and then by parameterizing melting reaction stoichiometries for isobaric slices in  $P$ - $F$  space. For any given pressure slice, the modal abundance of any given phase at any given  $F$  will be governed by a combination of the initial mode at the solidus (at the given  $P$ ), and the extent of melting at the given  $P$  required to exhaust the phase from the residue (defined by phase boundary curves in  $P$ - $F$  space). Thus, the basic requirements for parameterizing the mineral modes as a function of pressure and melt depletion are the pressure-dependent solidus modes and the extents of melting necessary to exhaust a mineral phase at any given pressure.

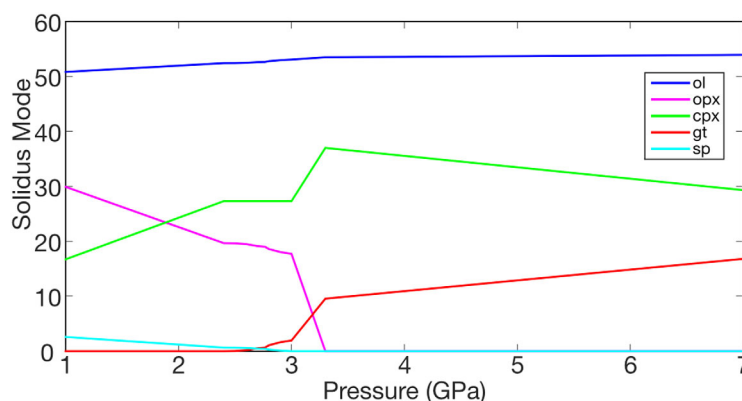


Figure B1. Parameterized solidus modes for pyrolite peridotite as a function of pressure.

### B1. Pyrolite Mineral Mode Evolution Parameterization

#### B1.1. Pyrolite Solidus Modes Parameterization

We have parameterized the solidus modes of pyrolite from 1 to 7 GPa using the experiments of Baker and Stolper [1994], Baker *et al.* [1995], Walter [1998], and Falloon *et al.* [1999], assuming that the bulk compositions of Kettle River

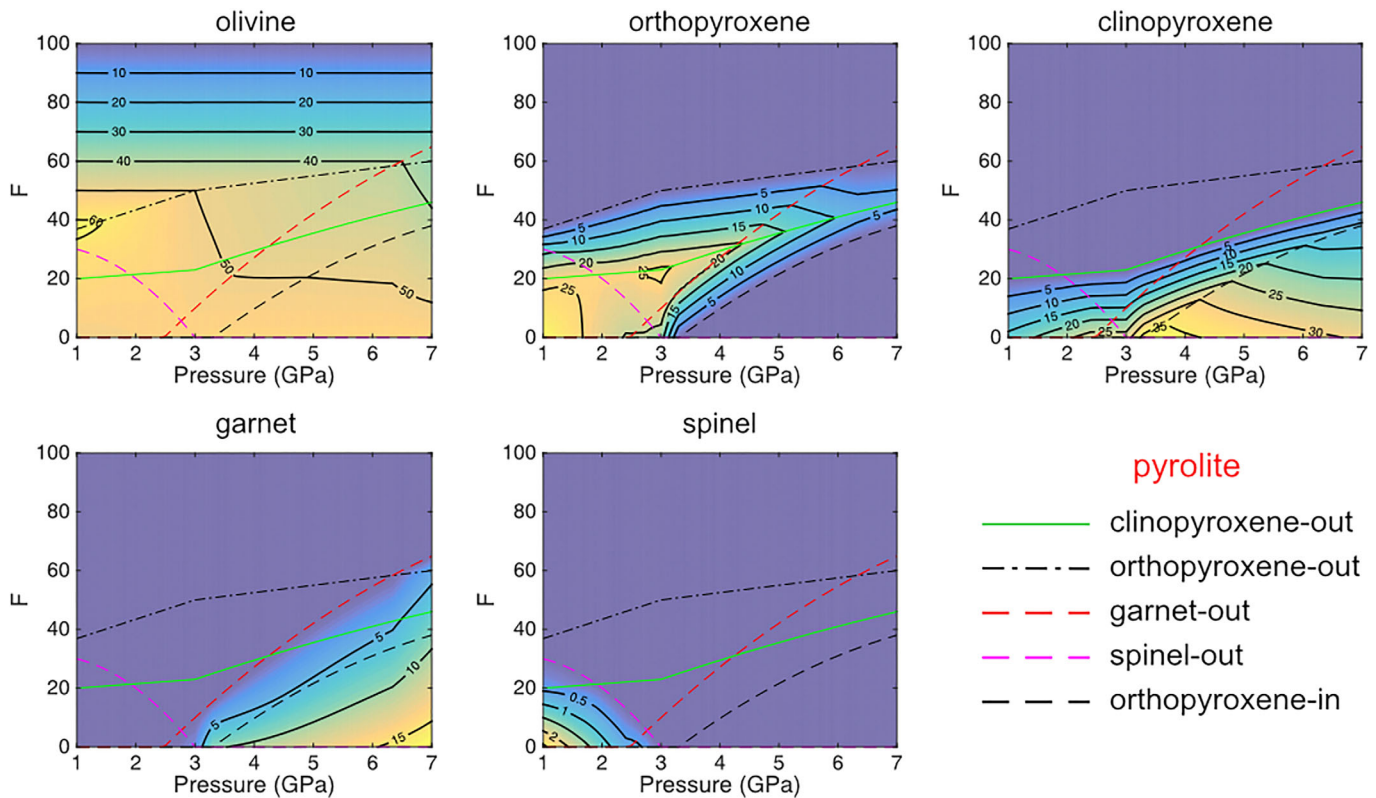


Figure B2. Parameterized phase boundary curves and mineral modes for pyrolite peridotite as a function of pressure and extent of melting.

peridotite (KR4003) and MM3 are similar enough to capture the pressure and melt depletion effects for pyrolite (as was done by Kimura and Kawabata [2014]). It is convenient to parameterize the solidus modes over discrete pressure ranges given the stability of the aluminous phases and orthopyroxene. For  $3.3 < P \leq 7$  GPa, the parameterized solidus modes are linear functions of  $P$  (in GPa)

$$\begin{aligned}
 ol_{solidus}^{pyrolite} &= 0.12P + 53.08 \\
 opx_{solidus}^{pyrolite} &= 0 \\
 cpx_{solidus}^{pyrolite} &= -2.08P + 43.86 \\
 sp_{solidus}^{pyrolite} &= 0 \\
 gt_{solidus}^{pyrolite} &= 1.96P + 3.06.
 \end{aligned}
 \tag{B1–B5}$$

Shallower than 3.3 GPa, orthopyroxene becomes stable on the solidus [e.g., Walter, 1998]. Thus, for  $3 \leq P \leq 3.3$  GPa

$$\begin{aligned}
 ol_{solidus}^{pyrolite} &= 1.4P + 48.85 \\
 opx_{solidus}^{pyrolite} &= -59P + 194.7 \\
 cpx_{solidus}^{pyrolite} &= 32.33P - 69.7 \\
 sp_{solidus}^{pyrolite} &= 0 \\
 gt_{solidus}^{pyrolite} &= 25.27P - 73.85.
 \end{aligned}
 \tag{B6–B10}$$

Between 1 and 2.3 GPa, where spinel is stable and garnet is not,

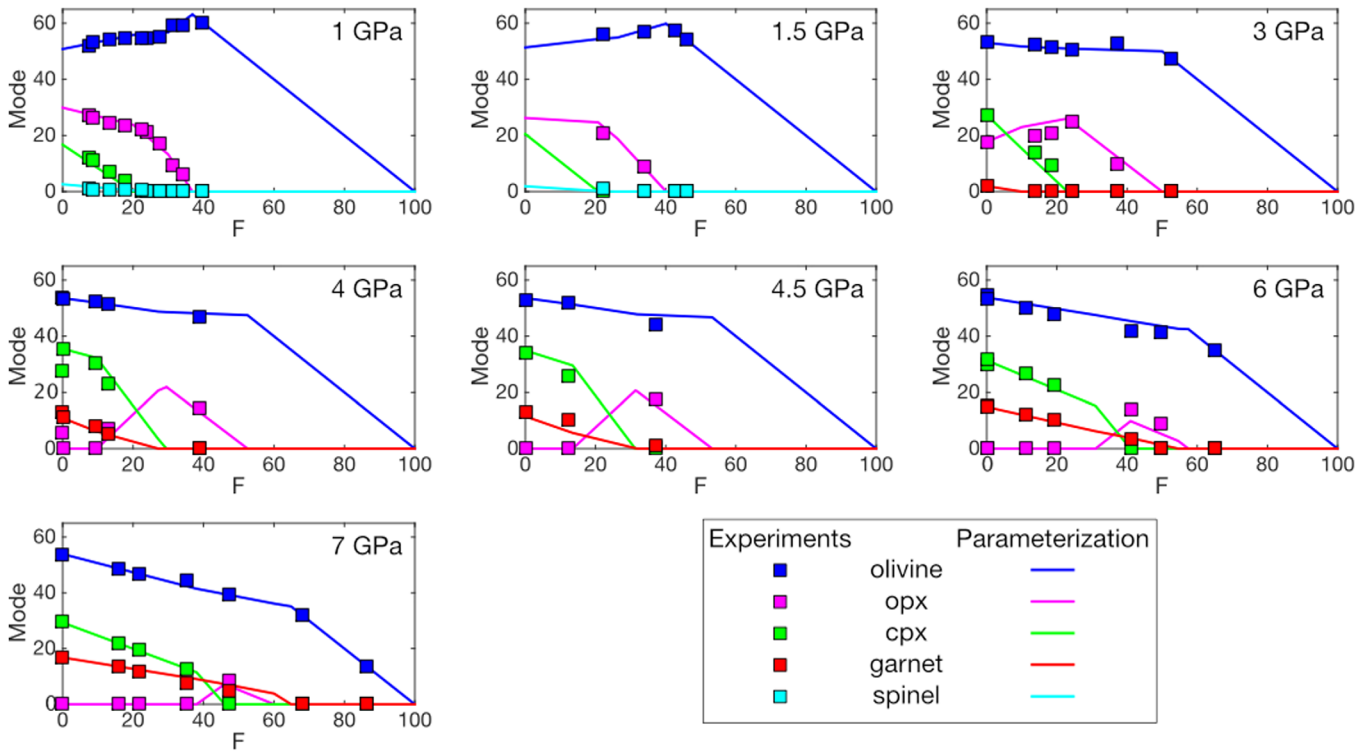


**Figure B3.** Comparison of parameterized pyrolite peridotite mineral modes as a function of melt depletion compared to melting experiments at 1, 1.5, 3, 4, 4.5, 6, and 7 GPa. For 1 and 1.5 GPa, experimental data are for the MM3 bulk composition [Baker and Stolper, 1994; Falloon et al., 1999]. For 3–7 GPa, experimental data are for the KR4003 bulk composition [Walter, 1998].

$$\begin{aligned}
 ol_{solidus}^{pyrolite} &= 1.14P + 49.66 \\
 opx_{solidus}^{pyrolite} &= -7.32P + 37.22 \\
 cpx_{solidus}^{pyrolite} &= 7.57P + 9.13 \\
 sp_{solidus}^{pyrolite} &= -1.39P + 3.99 \\
 gt_{solidus}^{pyrolite} &= 0.
 \end{aligned}
 \tag{B11–B15}$$

Calculating solidus modes becomes more involved where spinel and garnet coexist. Here we adopt the spinel-garnet reaction stoichiometry of Fram et al. [1998] between 2.3 and 3 GPa, giving the following parameterization for solidus mineral mode

$$\begin{aligned}
 ol_{solidus}^{pyrolite} &= ol_{solidus-1}^{pyrolite} - [1.667 - 0.556P]gt_{solidus-1}^{pyrolite} \\
 opx_{solidus}^{pyrolite} &= opx_{solidus-1}^{pyrolite} + [5 - 1.667P]gt_{solidus-1}^{pyrolite} \\
 cpx_{solidus}^{pyrolite} &= cpx_{solidus-1}^{pyrolite} \\
 sp_{solidus}^{pyrolite} &= sp_{solidus-1}^{pyrolite} + [1.667 - 0.556P]gt_{solidus-1}^{pyrolite} \\
 gt_{solidus}^{pyrolite} &= gt_{solidus-1}^{pyrolite} [1.667P - 4],
 \end{aligned}
 \tag{B16–B20}$$

where,  $ol_{solidus-1}^{pyrolite}$ ,  $opx_{solidus-1}^{pyrolite}$ ,  $cpx_{solidus-1}^{pyrolite}$ ,  $sp_{solidus-1}^{pyrolite}$ ,  $gt_{solidus-1}^{pyrolite}$  are mineral proportions for the previous decompression step. Pyrolite solidus modes are plotted as a function of pressure in Figure B1.

### B1.2. Pyrolite Phase Boundaries Parameterization

For pressures above 3 GPa, we parameterized the phase boundary locations (i.e., the amount of melting at a given pressure required to exhaust or crystallize a phase) based on the KR4003 experimental work of Walter [1998]. Below 3 GPa, phase boundary locations were estimated based on MM3 experimental results [Baker and Stolper, 1994; Baker et al., 1995; Falloon et al., 1999]. These boundaries include orthopyroxene-out, clinopyroxene-out,

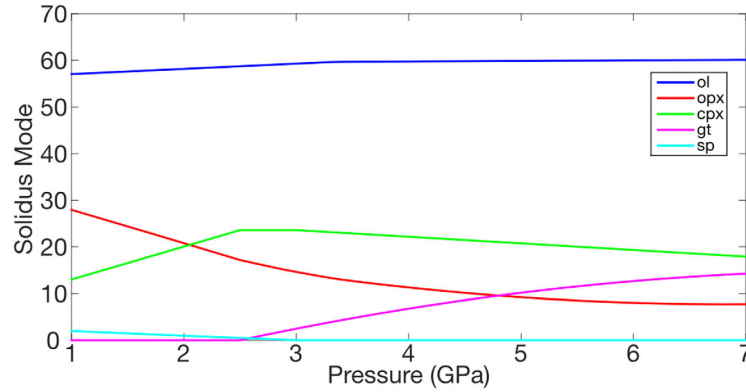


Figure B4. Parameterized solidus mode for DMM peridotite as a function of pressure.

spinel-out, garnet-out, and orthopyroxene-in (the olivine-out boundary is defined by the liquidus across all pressures). As with the solidus modes parameterization, it is convenient to parameterize the phase boundaries over discrete pressure intervals. The phase boundaries for orthopyroxene-out and clinopyroxene-out extend over the entire pressure range (1–7 GPa). For  $P \leq 3$  GPa, these boundaries, along with the spinel-out boundary, are

$$\begin{aligned}
 F_{opx-out}^{pyrolite} &= 6.58P + 30.28 \\
 F_{cpx-out}^{pyrolite} &= 1.5P + 18.5 \\
 F_{sp-out}^{pyrolite} &= -5P^2 + 5P + 30.
 \end{aligned} \tag{B21–B23}$$

For  $P > 3$  GPa, the orthopyroxene-out and clinopyroxene-out boundaries are

$$\begin{aligned}
 F_{opx-out}^{pyrolite} &= 2.5P + 42.5 \\
 F_{cpx-out}^{pyrolite} &= -0.25P^2 + 8.25P + 0.5.
 \end{aligned} \tag{B24–B25}$$

The garnet-out phase boundary for  $P \geq 2.4$  GPa is

$$F_{gt-out}^{pyrolite} = -1.16P^2 + 25.314P - 55.53, \tag{B26}$$

and the orthopyroxene-in phase boundary for  $P \geq 3.3$  GPa is

$$F_{opx-in}^{pyrolite} = -1.21P^2 + 22.75P - 61.87. \tag{B27}$$

Finally, for all  $P$ ,

$$F_{ol-out}^{pyrolite} = 100. \tag{B28}$$

Pyrolite phase boundaries are shown in Figure B2.

### B1.3. Pyrolite Melting Reaction Stoichiometries Parameterization

To quantify the effects of melt depletion, we calculated the melting reaction coefficients between 0 and 100%  $F$  from 1 to 7 GPa every 0.1 GPa. Mass balance dictates that at any given  $P$ , the amount a phase is produced (e.g., orthopyroxene at  $P > 3.3$  GPa) [Walter, 1998] or consumed (as governed by the melting reaction coefficients) between the solidus and liquidus must be equivalent to the mode of that phase at the solidus (at that  $P$ ). Thus, the sum of the product of the melting reaction coefficients for a given phase (e.g.,  $ol_{rxn1}^{pyrolite}$ ) and the  $F$ -interval ( $\Delta F$ ) between each phase boundary (e.g., at 1 GPa,  $\Delta F_1^{pyrolite} = F_{rxn1}^{pyrolite} - F_{cpx-out}^{pyrolite}$ ;  $\Delta F_2^{pyrolite} = F_{sp-out}^{pyrolite} - F_{cpx-out}^{pyrolite}$ ;  $\Delta F_3^{pyrolite} = F_{opx-out}^{pyrolite} - F_{sp-out}^{pyrolite}$ ; and  $\Delta F_4^{pyrolite} = F_{ol-out}^{pyrolite} - F_{opx-out}^{pyrolite}$ ) must equal the solidus mode of that phase (e.g.,  $ol_{solidus}^{pyrolite}$ )

$$\begin{bmatrix}
 ol_{rxn1}^{pyrolite} & ol_{rxn2}^{pyrolite} & ol_{rxn3}^{pyrolite} & ol_{rxn4}^{pyrolite} & ol_{rxn5}^{pyrolite} \\
 opx_{rxn1}^{pyrolite} & opx_{rxn2}^{pyrolite} & opx_{rxn3}^{pyrolite} & opx_{rxn4}^{pyrolite} & opx_{rxn5}^{pyrolite} \\
 cpx_{rxn1}^{pyrolite} & cpx_{rxn2}^{pyrolite} & cpx_{rxn3}^{pyrolite} & cpx_{rxn4}^{pyrolite} & cpx_{rxn5}^{pyrolite} \\
 sp_{rxn1}^{pyrolite} & sp_{rxn2}^{pyrolite} & sp_{rxn3}^{pyrolite} & sp_{rxn4}^{pyrolite} & sp_{rxn5}^{pyrolite} \\
 gt_{rxn1}^{pyrolite} & gt_{rxn2}^{pyrolite} & gt_{rxn3}^{pyrolite} & gt_{rxn4}^{pyrolite} & gt_{rxn5}^{pyrolite}
 \end{bmatrix} \cdot \begin{bmatrix}
 \Delta F_1^{pyrolite} \\
 \Delta F_2^{pyrolite} \\
 \Delta F_3^{pyrolite} \\
 \Delta F_4^{pyrolite} \\
 \Delta F_5^{pyrolite}
 \end{bmatrix} = \begin{bmatrix}
 ol_{solidus}^{pyrolite} \\
 opx_{solidus}^{pyrolite} \\
 cpx_{solidus}^{pyrolite} \\
 sp_{solidus}^{pyrolite} \\
 gt_{solidus}^{pyrolite}
 \end{bmatrix}. \tag{B29}$$

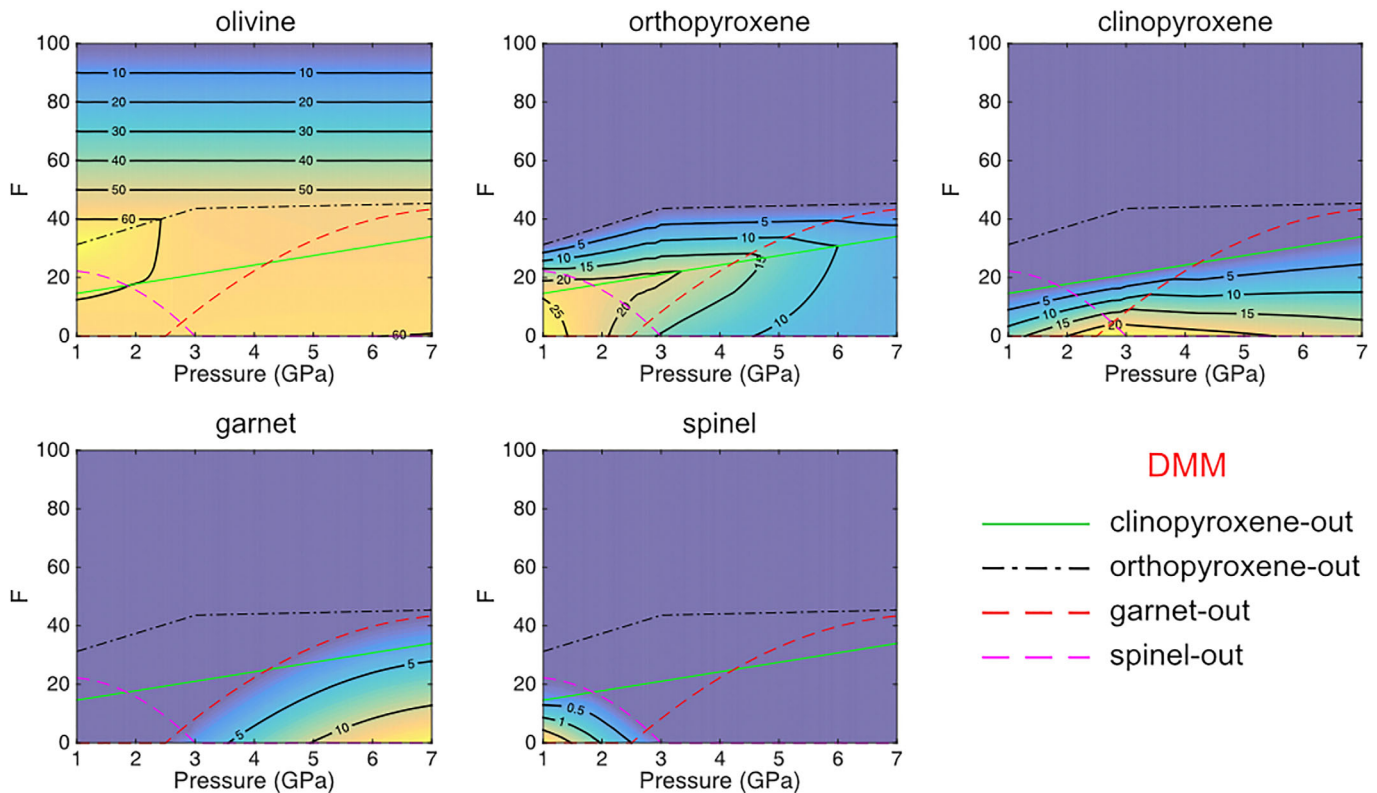


Figure B5. Parameterized phase boundary curves and mineral modes for DMM peridotite as a function of pressure and extent of melting.

An additional constraint from mass balance is that melting reaction coefficients within each melting interval ( $\Delta F$ ) at any given  $P$  must sum to unity. For example, at 1 GPa, equation (B29) yields

$$\begin{aligned}
 ol_{rxn1}^{pyrolite} \Delta F_1^{pyrolite} + ol_{rxn2}^{pyrolite} \Delta F_2^{pyrolite} + ol_{rxn3}^{pyrolite} \Delta F_3^{pyrolite} + ol_{rxn4}^{pyrolite} \Delta F_4^{pyrolite} &= ol_{solidus}^{pyrolite} \\
 opx_{rxn1}^{pyrolite} \Delta F_1^{pyrolite} + opx_{rxn2}^{pyrolite} \Delta F_2^{pyrolite} + opx_{rxn3}^{pyrolite} \Delta F_3^{pyrolite} + opx_{rxn4}^{pyrolite} \Delta F_4^{pyrolite} &= opx_{solidus}^{pyrolite} \\
 cpx_{rxn1}^{pyrolite} \Delta F_1^{pyrolite} + cpx_{rxn2}^{pyrolite} \Delta F_2^{pyrolite} + cpx_{rxn3}^{pyrolite} \Delta F_3^{pyrolite} + cpx_{rxn4}^{pyrolite} \Delta F_4^{pyrolite} &= cpx_{solidus}^{pyrolite} \\
 sp_{rxn1}^{pyrolite} \Delta F_1^{pyrolite} + sp_{rxn2}^{pyrolite} \Delta F_2^{pyrolite} + sp_{rxn3}^{pyrolite} \Delta F_3^{pyrolite} + sp_{rxn4}^{pyrolite} \Delta F_4^{pyrolite} &= sp_{solidus}^{pyrolite}
 \end{aligned}
 \tag{B30}$$

where

$$\begin{aligned}
 ol_{rxn1}^{pyrolite} + opx_{rxn1}^{pyrolite} + cpx_{rxn1}^{pyrolite} + sp_{rxn1}^{pyrolite} &= 1 \\
 ol_{rxn2}^{pyrolite} + opx_{rxn2}^{pyrolite} + cpx_{rxn2}^{pyrolite} + sp_{rxn2}^{pyrolite} &= 1 \\
 ol_{rxn3}^{pyrolite} + opx_{rxn3}^{pyrolite} + cpx_{rxn3}^{pyrolite} + sp_{rxn3}^{pyrolite} &= 1 \\
 ol_{rxn4}^{pyrolite} + opx_{rxn4}^{pyrolite} + cpx_{rxn4}^{pyrolite} + sp_{rxn4}^{pyrolite} &= 1.
 \end{aligned}
 \tag{B31}$$

Because the solution to equation (B29) is nonunique, we begin the parameterization at 1 GPa using melting reaction coefficients of Baker and Stolper [1994] as initial estimates. Given our modeled solidus modes and phase boundary locations, the Baker and Stolper [1994] melting reaction coefficients produce small misfits between the calculated modes (left-hand side of equation (B29)) and the modeled solidus modes. Using the Excel Solver, we optimized the melting reaction coefficients to minimize the misfits. We then take these “optimized” melting reaction coefficients and use them as an initial guess for the 1.1 GPa melting reaction coefficients. Because of the slight differences in modeled solidus modes and phase boundary locations at 1.1 GPa (compared with 1 GPa), these 1 GPa “optimized” melting reaction coefficients lead to a slight misfit between the calculated solidus modes at 1.1 GPa and the modeled solidus modes. We thus optimized the 1.1 GPa melting reaction coefficients using the Excel Solver and applied these as an initial guess for the

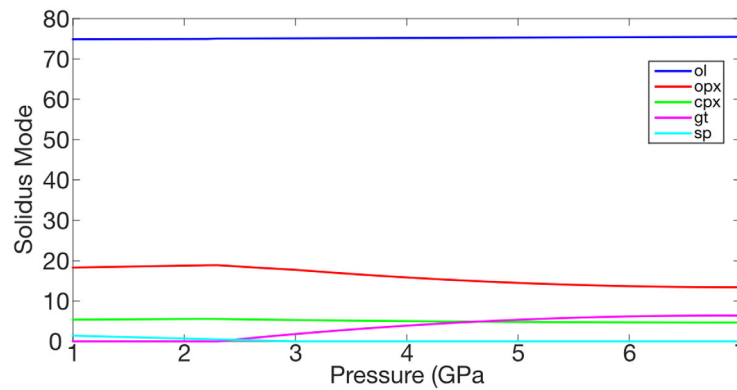


Figure B6. Parameterized solidus mode for harzburgite as a function of pressure.

melting reaction coefficients at 1.2 GPa. In this manner, we optimized the melting reaction coefficients every 0.1 GPa from 1 to 7 GPa. The resulting mineral modes as a function of  $P$  and  $F$  are shown in Figure B2. Moreover, Figure B3 shows that our parameterization provides good fits to experimental mineral modes as a function of melt fraction over the entire pressure range. Importantly, the

approach we have taken captures key features of the experimental data set, such as the low- $P$  peritectic reaction producing olivine with increasing  $F$  for  $P < 2$  GPa, and orthopyroxene production at higher pressures.

The mineral mode parameterization is programmed as a look-up table in REEBOX PRO, and residue mineral modes are calculated in the model by interpolation using the  $F$  and  $P$  defined by the melting path described in the main text. Melting reaction coefficients specified in equation (7) of the main text are similarly quantified by interpolation for the  $F$  and  $P$  along the melting path. Finally, this mineral mode parameterization allows the implementation of the Katz *et al.* [2003] peridotite melting parameterization, as  $F_{cpx-out}$ , which is a key parameter in the Katz *et al.* model, is given by equations (B22) and (B25) above.

## B2. Depleted MORB Mantle (DMM) Mineral Mode Evolution Parameterization

### B2.1. DMM Solidus Modes Parameterization

To simulate changes in the mineral assemblage for depleted MORB mantle (DMM) as a function of  $P$  and  $F$ , we first parameterized solidus modes that are consistent with DMM solidus modes estimated by Workman and Hart [2005] using the Stixrude and Lithgow-Bertelloni [2011] thermodynamic database in *Perple\_X* [Connolly, 1990, 2005] between 1 and 7 GPa (Figure B4). We used *Perple\_X* to parameterize DMM solidus modes because experimental constraints on the DMM bulk composition are lacking. Our parameterized DMM solidus olivine mode is

$$ol_{solidus}^{DMM} = 1.12P + 55.92 \tag{B32}$$

for  $P < 3.3$  GPa, and

$$ol_{solidus}^{DMM} = 0.12P + 59.28 \tag{B33}$$

for  $P \geq 3.3$  GPa. Our parameterized clinopyroxene mode along the DMM solidus is

$$cpx_{solidus}^{DMM} = 7.07P + 5.93 \tag{B34}$$

for  $P < 2.6$  GPa, and

$$cpx_{solidus}^{DMM} = 23.6 \tag{B35}$$

for  $2.6 \leq P \leq 3$  GPa, and

$$cpx_{solidus}^{DMM} = -1.42P + 27.87 \tag{B36}$$

for  $P > 3$  GPa. The spinel mode, which is stable for  $P < 3$  GPa, is

$$sp_{solidus}^{DMM} = 0.06P^2 - 1.21P + 3.16, \tag{B37}$$

and above 2.5 GPa, the parameterized garnet mode along the solidus is

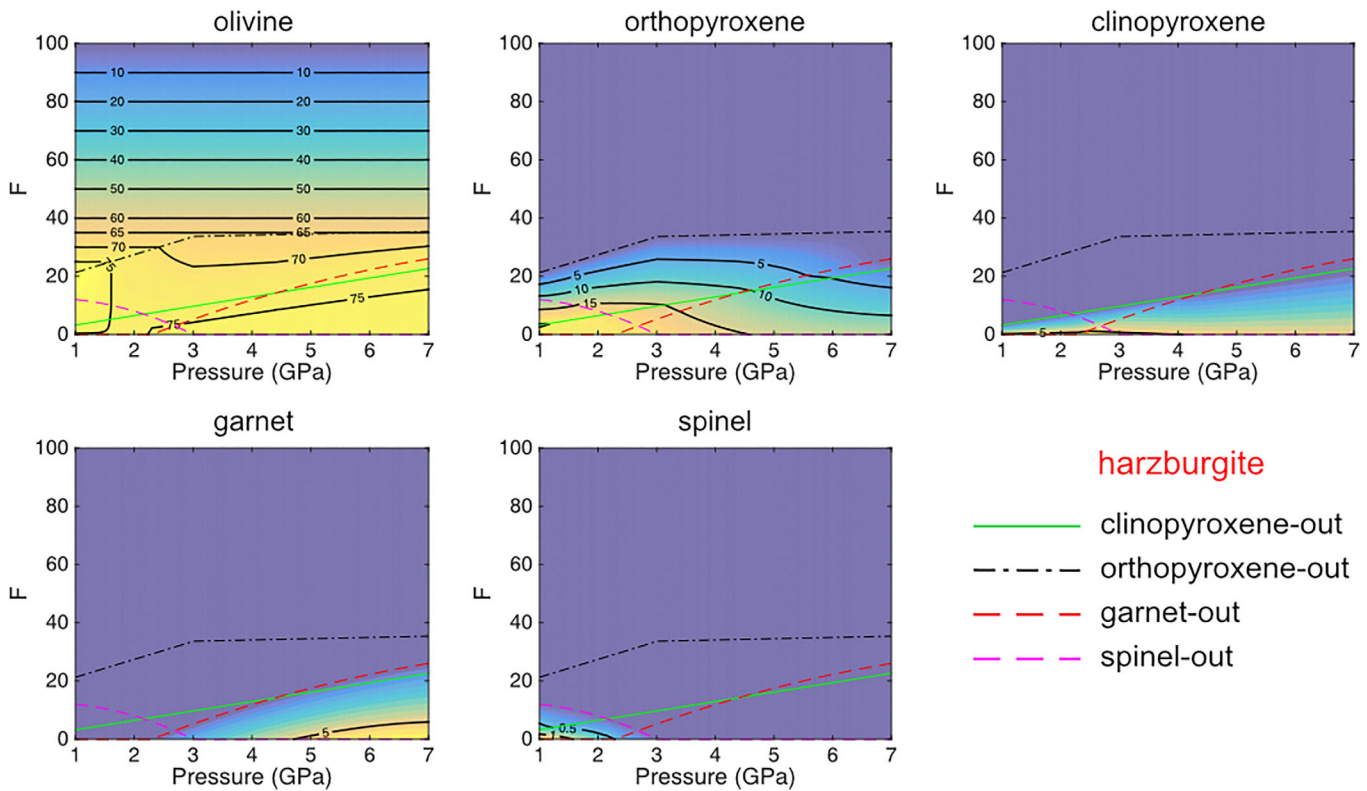


Figure B7. Parameterized phase boundary curves and mineral modes for harzburgite as a function of pressure and extent of melting.

$$g_{solidus}^{DMM} = -0.45P^2 + 7.43P - 15.76. \tag{B38}$$

For all  $P$ , the solidus mode of orthopyroxene is calculated by difference after summing the modal abundance for all other phases present at the solidus. In contrast to our modeled pyrolite composition, orthopyroxene remains stable along the DMM solidus across the entire pressure range (1–7 GPa).

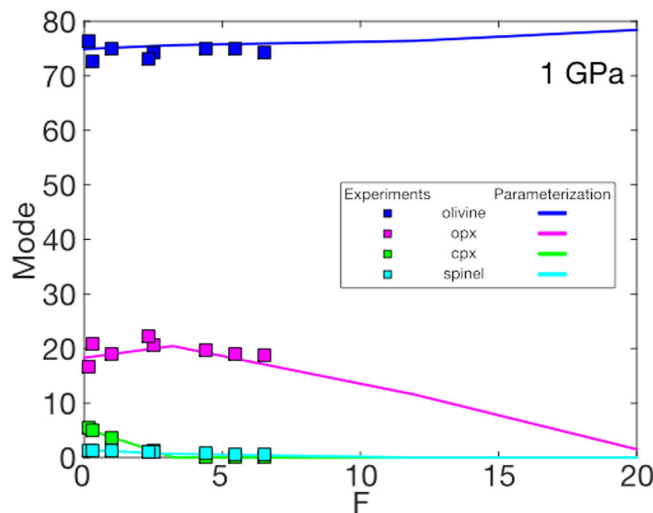


Figure B8. Comparison of parameterized harzburgite mineral modes as a function of melt depletion compared to melting experiments at 1 GPa for the Depma harzburgite bulk composition [Laporte et al., 2004].

### B2.2. DMM Phase Boundaries and Melting Reaction Coefficients Parameterizations

To model the phase boundary locations and melting reaction coefficients for DMM, we draw on the fact that experimentally determined melting reaction coefficients for depleted bulk compositions (DMM1 [Wasylenki et al., 2003]; Tinaquillo Iherzolite [Robinson et al., 1998]) are similar to those for more fertile peridotite compositions at 1 and 1.5 GPa. Thus, we initially applied our parameterized pyrolite melting reaction coefficients and phase boundary locations for all  $P$  while using our parameterized DMM solidus modes. Based on the misfits between the calculated modes and

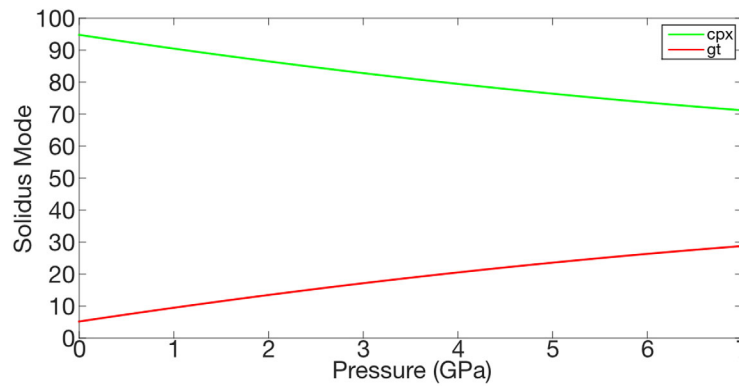


Figure B9. Parameterized solidus mode for G2 pyroxenite as a function of pressure.

$$F_{cpx-out}^{DMM} = 3.24P + 11.37. \tag{B39}$$

while for  $P \leq 3$  GPa the spinel-out and orthopyroxene-out phase boundaries are

$$F_{sp-out}^{DMM} = -4.6P^2 + 7.33P + 19.52 \tag{B40}$$

$$F_{opx-out}^{DMM} = 6.15P + 25.1. \tag{B41}$$

For  $P > 3$  GPa, the orthopyroxene-out phase boundary is

$$F_{opx-out}^{DMM} = 0.43P + 42.35, \tag{B42}$$

and for  $P > 2.5$  GPa, the garnet-out phase boundary is

$$F_{gt-out}^{DMM} = -1.74P^2 + 26.18P - 54.56, \tag{B43}$$

For all  $P$ ,

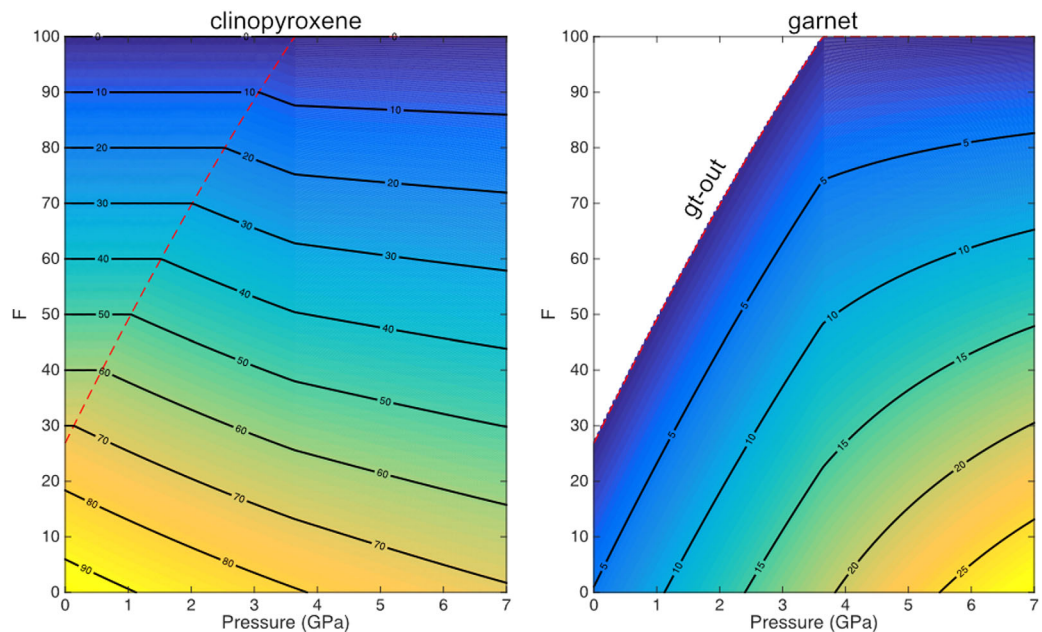
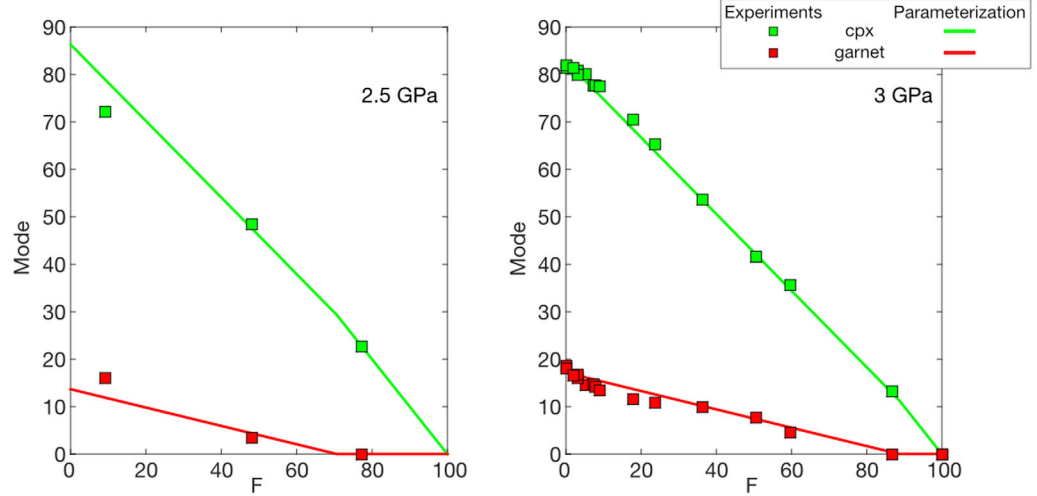


Figure B10. Parameterized garnet-out boundary curve (red-dashed curve) and mineral modes for G2 pyroxenite as a function of pressure and extent of melting.



**Figure B11.** Comparison of parameterized G2 mineral modes as a function of melt depletion compared to melting experiments at 2.5 and 3 GPa for the G2 pyroxenite bulk composition [Pertermann and Hirschmann, 2003a,b].

$$F_{ol-out}^{DMM} = 100. \tag{B44}$$

Phase boundaries and modes as a function of  $P$  and  $F$  for DMM are shown in Figure B5.

### B3. Harzburgite Mineral Mode Evolution Parameterization

#### B3.1. Harzburgite Solidus Modes Parameterization

To simulate the mineral mode evolution of harzburgite as a function of  $P$  and  $F$ , we again used the *Stixrude and Lithgow-Bertelloni* [2011] database in *Perple\_X* [Connolly, 1990, 2005] to parameterize the solidus modes of Depma harzburgite [Laporte et al., 2004]. For  $P \leq 2.2$  GPa, the olivine and clinopyroxene solidus modes are

$$\begin{aligned} ol_{solidus}^{harzburgite} &= 0.0553P + 74.86 \\ cpx_{solidus}^{harzburgite} &= 0.1643P + 5.22, \end{aligned} \tag{B45–B46}$$

and for  $P > 2.2$  GPa

$$\begin{aligned} ol_{solidus}^{harzburgite} &= 0.0931P + 74.85 \\ cpx_{solidus}^{harzburgite} &= 0.0419P^2 - 0.5741P + 6.65. \end{aligned} \tag{B47–B48}$$

At  $P \leq 3$  GPa where spinel is stable

$$sp_{solidus}^{harzburgite} = -0.7P + 2.1, \tag{B49}$$

while for  $P \geq 2.3$  GPa where garnet is stable

$$gt_{solidus}^{harzburgite} = -0.3125P^2 + 4.27P - 8.179. \tag{B50}$$

Again, at each pressure the orthopyroxene mode is calculated by difference based on the sum of other phases at the solidus. Modeled harzburgite solidus modes as a function of pressure are shown in Figure B6.

#### B3.2. Harzburgite Phase Boundaries and Melting Reaction Coefficients Parameterizations

To model the phase boundary locations and melting reaction coefficients for harzburgite, we followed the same approach as used for DMM. We initially applied our DMM melting reaction coefficients and phase boundary locations for all  $P$  in conjunction with our parameterized harzburgite solidus modes. Based on the misfits between the calculated modes and our parameterized harzburgite solidus modes, we iteratively adjusted the phase boundary locations and melting reaction coefficients until the misfits were minimized.

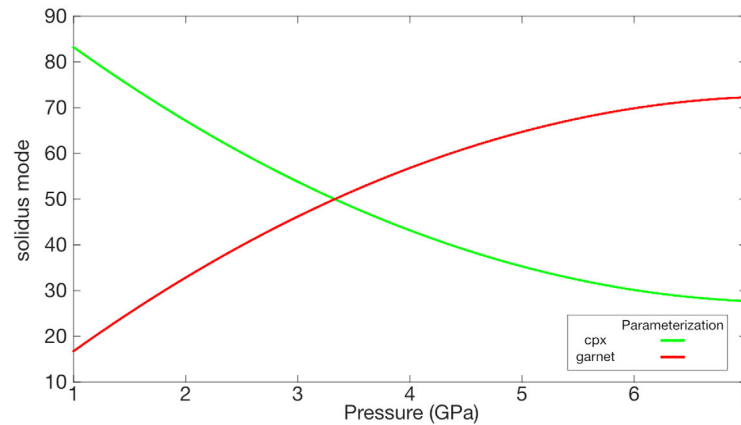


Figure B12. Parameterized solidus mode for MIX1G pyroxenite as a function of pressure.

In the absence of experimental constraints on harzburgite bulk compositions over a wide range of pressures, we maintained the same general functional forms for the phase boundaries as used in our DMM parameterization.

For  $P < 2.9$  GPa, the parameterized orthopyroxene-out phase boundary is

$$F_{opx-out}^{harzburgite} = 6.15P + 15.1, \tag{B51}$$

and for  $P \geq 2.9$  GPa

$$F_{opx-out}^{harzburgite} = 0.43P + 32.35. \tag{B52}$$

The spinel-out phase boundary for  $P \leq 3$  GPa is

$$F_{sp-out}^{harzburgite} = -2P^2 + 2P + 12 \tag{B53}$$

and the garnet-out phase boundary for  $P \geq 2.3$  GPa is

$$F_{gt-out}^{harzburgite} = -0.479P^2 + 9.98P - 20.43. \tag{B54}$$

For all  $P$ , the clinopyroxene-out and olivine-out phase boundaries are

$$F_{cpx-out}^{harzburgite} = 3.24P \tag{B55}$$

$$F_{ol-out}^{harzburgite} = 100. \tag{B56}$$

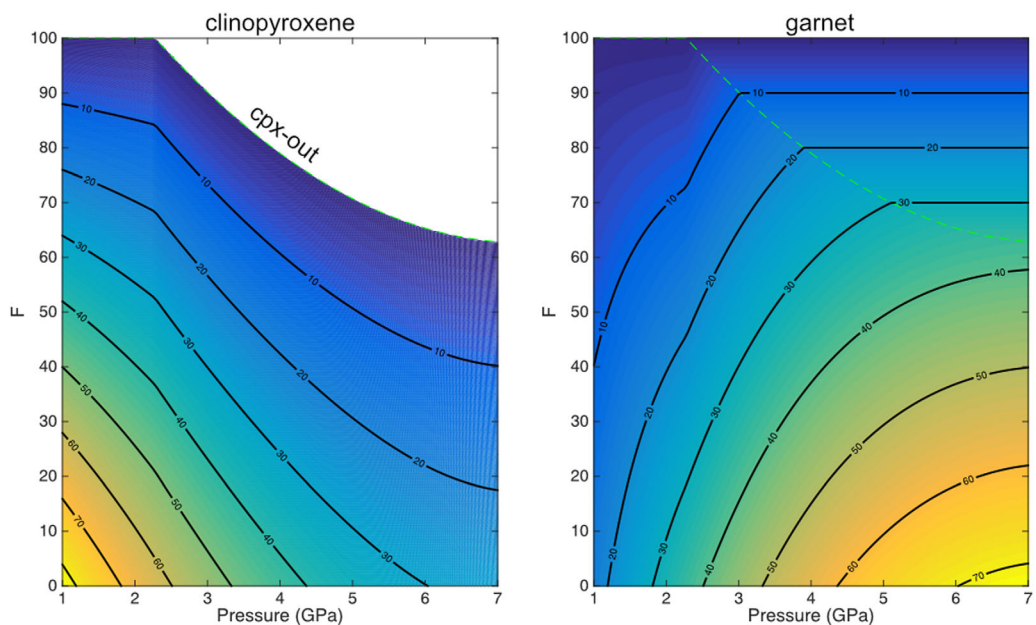
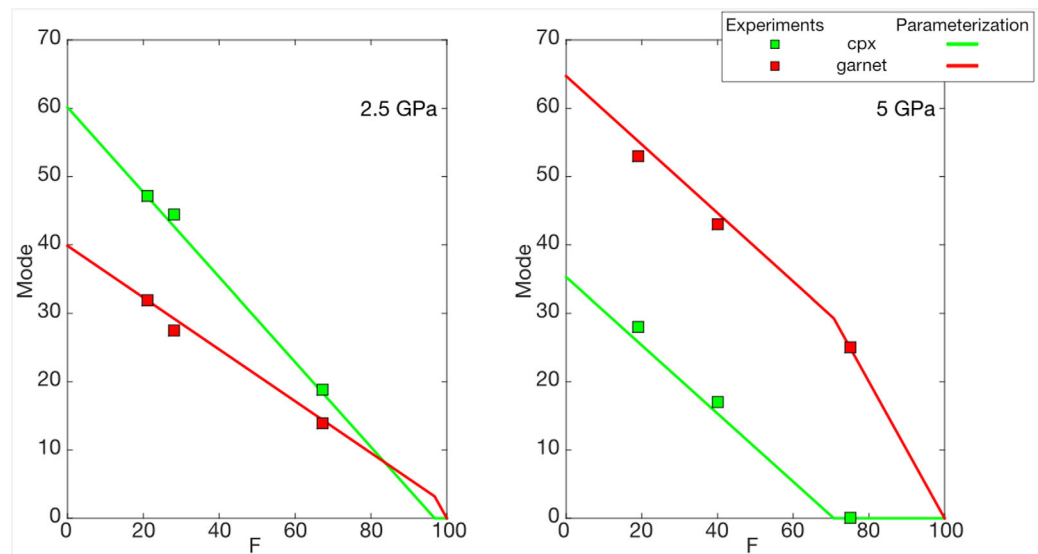


Figure B13. Parameterized clinopyroxene-out boundary curve (green-dashed curve) and mineral modes for MIX1G pyroxenite as a function of pressure and extent of melting.



**Figure B14.** Comparison of parameterized MIX1G mineral modes as a function of melt depletion compared to melting experiments at 2.5 and 5 GPa for the MIX1G pyroxenite bulk composition [Hirschmann et al., 2003; Kogiso et al., 2003].

Parameterized boundary curves and mineral modes for harzburgite are shown in Figure B7. As shown in Figure B8, these parameterized modes compare well with existing experimental data on Depma harzburgite at 1 GPa [Laporte et al., 2004].

## B4. G2 Pyroxenite Mineral Mode Evolution Parameterization

### B4.1. G2 Pyroxenite Solidus Modes Parameterization

To model the mineral modes of G2 pyroxenite as a function of  $P$  and  $F$ , we make the simplifying assumption that pyroxenite consisting only of clinopyroxene and garnet. We parameterized solidus modes from 2 to 7 GPa using the *Stixrude and Lithgow-Bertelloni* [2011] database in *Perple\_X* [Connolly, 1990, 2005] (we chose the minimum pressure of 2 GPa because plagioclase becomes stable on the solidus at  $P < 2$  GPa). We parameterized the clinopyroxene and garnet solidus modes using second-order polynomials, but adjusted the intercepts to better match the experimental modes at 3 GPa [Pertermann and Hirschmann, 2003a,b]. Assuming these parameterizations can be extrapolated across all  $P$  between 1 and 7 GPa, the clinopyroxene and garnet solidus modes are (Figure B9)

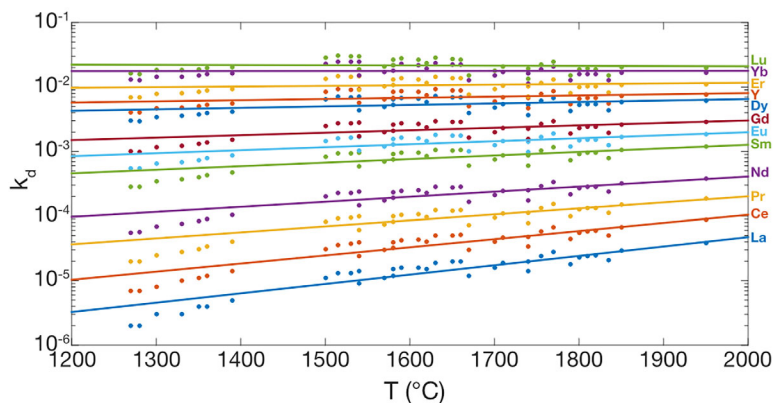


**Figure C1.** Parameterizing calculated olivine-melt partition coefficients for the rare-earth elements and Y as a function of temperature. Olivine mineral-melt partition coefficients were calculated for the pressures, temperatures, and compositions of peridotite melts and coexisting olivine from peridotite melting experiments [Baker and Stolper, 1994; Walter, 1998; Falloon et al., 1999] using the lattice strain model of Sun and Liang [2013, 2014]. These olivine-melt partition coefficients are parameterized as a function of temperature using an equation of the form  $k_{d,olivine}^{element} = a \exp(bT)$  (colored curves).

**Table C1.** Regression Coefficients for Temperature-Dependent Olivine Mineral-Melt Partition Coefficients<sup>a</sup>

Element	a	b
La	$5.96 \times 10^{-8}$	$3.34 \times 10^{-3}$
Ce	$3.22 \times 10^{-7}$	$2.89 \times 10^{-3}$
Pr	$2.82 \times 10^{-6}$	$2.14 \times 10^{-3}$
Nd	$1.12 \times 10^{-5}$	$1.80 \times 10^{-3}$
Sm	$9.96 \times 10^{-5}$	$1.27 \times 10^{-3}$
Eu	$2.35 \times 10^{-4}$	$1.07 \times 10^{-3}$
Gd	$5.26 \times 10^{-4}$	$8.76 \times 10^{-4}$
Dy	$2.28 \times 10^{-3}$	$5.23 \times 10^{-4}$
Y	$3.45 \times 10^{-3}$	$4.23 \times 10^{-4}$
Er	$7.46 \times 10^{-3}$	$2.21 \times 10^{-4}$
Yb	$1.74 \times 10^{-2}$	$9.87 \times 10^{-6}$
Lu	$2.42 \times 10^{-2}$	$-7.24 \times 10^{-5}$

$${}^a k_{\text{olivine}}^{\text{element}} = a \exp(bT).$$

$$\begin{aligned} cpx_{\text{solidus}}^{G2} &= 0.155P^2 - 4.454P + 94.8 \\ gt_{\text{solidus}}^{G2} &= 0.155P^2 + 4.454P + 5.2. \end{aligned} \quad (\text{B57–B58})$$

## B4.2. G2 Pyroxenite Phase Boundaries and Melting Reaction Coefficients Parameterizations

To parameterize the melting reaction coefficients for clinopyroxene and garnet as a function of  $P$  and  $F$ , we again rely on experiments [Pertermann and Hirschmann, 2003a,b]. We find that for  $P > 3.64$  GPa, garnet and clinopyroxene are both saturated at the liquidus, so that

$$\begin{aligned} F_{\text{cpx-out}}^{G2} &= 100 \\ F_{\text{gt-out}}^{G2} &= 100. \end{aligned} \quad (\text{B59–B60})$$

For  $P < 3.64$  GPa, only clinopyroxene is saturated at the liquidus (i.e.,  $F_{\text{cpx-out}}^{G2} = 100$ ), while

$$F_{\text{gt-out}}^{G2} = -0.8P^2 + 23.02P + 26.85. \quad (\text{B61})$$

For all  $P$  and  $F < F_{\text{gt-out}}^{G2}$ , we determine the appropriate melting reaction coefficients for garnet from mass balance,

$$gt_{\text{rxn}}^{G2} = \frac{gt_{\text{solidus}}^{G2}}{F_{\text{gt-out}}^{G2}}. \quad (\text{B62})$$

while for  $F \geq F_{\text{gt-out}}^{G2}$ ,

$$gt_{\text{rxn}}^{G2} = 0. \quad (\text{B63})$$

Finally, mass balance requires that

$$cpx_{\text{rxn}}^{G2} = 1 - gt_{\text{rxn}}^{G2}. \quad (\text{B64})$$

G2 mineral modes as a function of pressure and melt depletion are shown in Figure B10. As shown in Figure B11, our predicted G2 mineral modes as a function of melt fraction agree well with experiments at 2 and 3 GPa [Pertermann and Hirschmann, 2003a,b].

## B5. MIX1G Pyroxenite Mineral Mode Evolution Parameterization

### B5.1. MIX1G Pyroxenite Solidus Modes Parameterization

To parameterize MIX1G pyroxenite mineral modes as a function of  $P$  and  $F$ , we again made the simplifying assumption that MIX1G consists solely of clinopyroxene and garnet. We parameterized the clinopyroxene and garnet solidus modes from 1–7 GPa using the *Stixrude and Lithgow-Bertelloni* [2011] database in *Perple\_X* [Connolly, 1990, 2005] using second order polynomials, but adjusted the intercepts to better match the experimental modes at 2.5 and 5 GPa [Hirschmann et al., 2003; Kogiso et al., 2003]. Assuming these parameterizations apply for  $P = 1–7$  GPa, the clinopyroxene and garnet solidus modes are (Figure B12)

$$\begin{aligned} cpx_{\text{solidus}}^{\text{MIX1G}} &= 1.366P^2 - 20.184P + 102.06 \\ gt_{\text{solidus}}^{\text{MIX1G}} &= 1.366P^2 + 20.184P - 2.06. \end{aligned} \quad (\text{B65–B66})$$

### B5.2. MIX1G Pyroxenite Phase Boundaries and Melting Reaction Coefficients Parameterizations

We determined the MIX1G melting reaction coefficients in a similar manner as with G2 pyroxenite. We started by calculating a  $P$ -dependent parameterization of the melting reactions from experiments conducted at 2.5 and 5 GPa [Hirschmann et al., 2003; Kogiso et al., 2003]. These experimentally-based parameterizations, combined with our parameterized solidus modes, indicate that  $F_{\text{cpx-out}}^{\text{MIX1G}} < 100\%$  for  $P > 2.25$  GPa. Thus, for  $P \geq 2.25$  GPa,

**Table C2.** Peridotite Mineral-Melt Partition Coefficients<sup>a</sup>

	ol	opx	cpx	sp	gt
Rb	0.00018	0.006	0.0007	0.0001	0.007
Ba	0.0003	0.0006	0.0007	0.0001	0.0007
Th	0.00001	0.001	0.00068	0.0024	0.0007
U	0.0004	0	0.0008	0.012	0.005
Nb	0.005	0.0031	0.0077	0.086	0.02
Ta	0.0005	0.004	0.01	0.08	0.015
K	0.00002	0.0001	0.001	0.0001	0.013
La	0.0004	0.002	0.0536	0.0012	0.01
Ce	0.0005	0.003	0.0858	0.0019	0.021
Pb	0.00001	0.0013	0.01	0	0.0005
Pr	0.001	0.0048	0.1	0.0023	0.045
Sr	0.00019	0.007	0.13	0.003	0.006
Nd	0.001	0.0068	0.19	0.01	0.087
Sm	0.001	0.01	0.29	0.007	0.217
Zr	0.01	0.01	0.12	0.56	0.32
Hf	0.005	0.01	0.26	0.65	0.32
Eu	0.002	0.013	0.47	0.01	0.4
Ti	0.02	0.024	0.38	0.048	0.2
Gd	0.002	0.016	0.48	0.016	0.498
Dy	0.002	0.022	0.44	0.01	1.06
Y	0.005	0.028	0.4	0.05	2.11
Er	0.002	0.03	0.39	0.01	3
Yb	0.0015	0.049	0.43	0.01	4.03
Lu	0.0015	0.06	0.43	0.28	5.5

<sup>a</sup>Data sources: McKenzie and O’Nions [1991, 1995], Horn et al. [1994], Salters and Stracke [2004], Klemme et al. [2006], Pilet et al. [2011].

$$F_{cpx-out}^{MIX1G} = 1.44P^2 - 21.23P + 140.87, \tag{B67}$$

and for  $P < 2.25$  GPa,

$$F_{cpx-out}^{MIX1G} = 100. \tag{B68}$$

For all  $P$ ,

$$F_{gt-out}^{MIX1G} = 100\%. \tag{B69}$$

As with the G2 melting reaction parameterization, we calculated the appropriate clinopyroxene melting reaction coefficients at every pressure using mass balance for  $F < F_{cpx-out}^{MIX1G}$

$$cpx_{rxn}^{MIX1G} = \frac{cpx_{solidus}^{MIX1G}}{F_{cpx-out}^{MIX1G}}. \tag{B70}$$

For  $F \geq F_{cpx-out}^{MIX1G}$

$$cpx_{rxn}^{MIX1G} = 0. \tag{B71}$$

As before, mass balance requires

$$gt_{rxn}^{MIX1G} = 1 - cpx_{rxn}^{MIX1G}. \tag{B72}$$

Phase boundaries and mineral modes for MIX1G as functions of  $P$  and  $F$  are shown in Figure B13. As shown in Figure B14, our estimates of MIX1G mineral modes as a function of melt fraction compare well with experiments at 2.5 and 5 GPa [Hirschmann et al., 2003; Kogiso et al., 2003].

### Appendix C: Peridotite Olivine-Melt Trace Element Partitioning Parameterization

In REEBOX PRO, lherzolite trace element partitioning can be modeled using the Kimura and Kawabata [2014] temperature-dependent parameterization for mineral-melt trace element partition coefficients. This parameterization uses the pressures, temperatures, and phase compositions from the peridotite melting experiments of Baker and Stolper [1994] and Walter [1998] to calculate mineral-melt partition coefficients for the rare earth elements (REE) and Y using lattice strain partitioning models [e.g., Wood and Blundy, 2003; Sun and Liang, 2013]. These REE and Y partition coefficients are regressed as a function of temperature to arrive at a  $T$ -dependent parameterization,

$$k_{dphase}^{element} = a \exp(bT), \tag{C1}$$

where  $a$  and  $b$  are regression constants, and  $T$  is in Celsius. Partition coefficients for the other trace elements in clinopyroxene and orthopyroxene were extrapolated by scaling the mineral-melt partition coefficients presented by Pilet et al. [2011] to the  $T$ -dependent partition coefficients for key REE (La, Sm, and Eu). A similar scaling was applied to garnet partitioning using the partition coefficients of McKenzie and O’Nions [1991, 1995].

**Table C3.** Pyroxenite Mineral-Melt Partition Coefficients<sup>a</sup>

	cpx	gt
Rb	0.0018	0.005
Ba	0.006	0.005
Th	0.0032	0.0008
U	0.0041	0.0045
Nb	0.005	0.005
Ta	0.011	0.004
K	0.03	0
La	0.027	0.012
Ce	0.055	0.005
Pb	0.042	0.056
Pr	0.11	0.011
Sr	0.067	0.01
Nd	0.122	0.057
Sm	0.19	0.19
Zr	0.1	0.19
Hf	0.22	0.22
Eu	0.179	0.208
Ti	0.38	0.25
Gd	0.318	0.584
Dy	0.42	1.72
Y	0.47	2.62
Er	0.51	3.42
Yb	0.55	5.71
Lu	0.56	7.03

<sup>a</sup>All partition coefficients are from Run A343 of Pertermann et al. [2004], except for Pr, which comes from Klemme et al. [2002].

For olivine-melt partitioning in peridotite, Kimura and Kawabata [2014] used the parameterization of Bédard [2005], which depends on the MgO content of the melt (which in turn depends on  $P$ ,  $T$ , and  $F$ ). However, we have not incorporated this parameterization because it predicts that light rare earth elements (La, Ce, Pr, Nd) are more compatible in olivine than Sm [see Kimura and Kawabata, 2014, Figure 4g]. This behavior is opposite of that predicted by lattice strain theory, where  $k_{\text{olivine}}^{\text{La}} < k_{\text{olivine}}^{\text{Ce}} < k_{\text{olivine}}^{\text{Nd}} < k_{\text{olivine}}^{\text{Sm}}$  [e.g., Wood and Blundy, 2003; Sun and Liang, 2013]. Furthermore, as noted by Bédard [2005], lattice strain theory is better suited to modeling olivine-melt elemental partitioning during decompression melting than the parameterization he presented.

To quantify  $T$ -dependent mineral-melt partition coefficients for olivine in peridotite, we applied the recent olivine-melt lattice strain model for the REE and Y presented by Sun and Liang [2013, 2014] to the peridotite melting experimental data sets of Baker and Stolper [1994] and Walter [1998], and have parameterized these olivine mineral-melt partition coefficients as a function of temperature, using equation (C1) (see Figure C1). The regressed values of the coefficients  $a$  and  $b$  for the REE and Y are provided in Table C1. We then extrapolated the partition coefficients for the non-REE elements by scaling the olivine-melt partition coefficients of Pilet *et al.* [2011] to the temperature-dependent coefficients for La, Sm, and Eu, as Kimura and Kawabata [2014] did for clinopyroxene. The non-temperature-dependent lherzolite and pyroxenite partition coefficients also included in REEBOX PRO (see main text) are given in Tables C2 and C3, respectively.

#### Acknowledgments

We thank Kenni D. Petersen for help with optimizing the code. This work has benefitted from thoughtful and constructive reviews by Andreas Stracke, Paul Asimow, and Keith Putirka. C.E.L. acknowledges support by the U.S. National Science Foundation under grant 0511049, and by the Danish National Research Foundation for the Niels Bohr Professorship at Aarhus University, DK. The data used in this study are available in the tables, appendices, and references.

#### References

- Allegre, C. J., and D. L. Turcotte (1986), Implications of a two-component marble-cake mantle, *Nature*, 323, 123–127, doi:10.1038/323123a0.
- Asimow, P. D., and C. H. Langmuir (2003), The importance of water to oceanic mantle melting regimes, *Nature*, 421, 815–820, doi:10.1038/nature01429.
- Asimow, P. D., M. M. Hirschmann, and E. M. Stolper (1997), An analysis of variations in isentropic melt productivity, *Philos. Trans. R. Soc. London A*, 355, 255–281, doi:10.1098/rsta.1997.0009.
- Asimow, P. D., M. M. Hirschmann, and E. M. Stolper (2001), Calculation of peridotite partial melting from thermodynamic models of minerals and melts, IV. Adiabatic decompression and the composition and mean properties of mid-ocean ridge basalts, *J. Petrol.*, 42, 963–998, doi:10.1093/ptology/42.5.963.
- Baker, M. B., and E. M. Stolper (1994), Determining the composition of high-pressure mantle melts using diamond aggregates, *Geochim. Cosmochim. Acta*, 58, 2811–2827, doi:10.1016/0016-7037(94)90116-3.
- Baker, M. B., M. M. Hirschmann, M. S. Ghiorso, and E. M. Stolper (1995), Compositions of near-solidus peridotite melts from experiments and thermodynamic calculations, *Nature*, 375, 308–311, doi:10.1038/375308a0.
- Bédard, J. H. (2005), Partitioning coefficients between olivine and silicate melts, *Lithos*, 83, 394–419, doi:10.1016/j.lithos.2005.03.011.
- Bourdon, B., J.-L. Joron, C. Claude-Ivanaj, and C. J. Allegre (1998), U–Th–Pa–Ra systematics for the Grande Comore volcanics: Melting processes in an upwelling plume, *Earth Planet. Sci. Lett.*, 164, 119–133, doi:10.1016/S0012-821X(98)00227-1.
- Bown, J. W., and R. S. White (1994), Variation with spreading rate of oceanic crustal thickness and geochemistry, *Earth Planet. Sci. Lett.*, 121, 435–449, doi:10.1016/0012-821X(94)90082-5.
- Brown, E. L., and C. E. Lesher (2014), North Atlantic magmatism controlled by temperature, mantle composition and buoyancy, *Nat. Geosci.*, 7, 820–824, doi:10.1038/ngeo2264.
- Chauvel, C., and C. Hémond (2000), Melting of a complete section of recycled oceanic crust: Trace element and Pb isotopic evidence from Iceland, *Geochim. Geophys. Geosyst.*, 1, 1001, doi:10.1029/1999GC000002.
- Connolly, J. A. D. (1990), Multivariable Phase Diagrams: An algorithm based on generalized thermodynamics, *Am. J. Sci.*, 290, 666–718, doi:10.2475/ajs.290.6.666.
- Connolly, J. A. D. (2005), Computation of phase equilibria by linear programming: A tool for geodynamic modeling and its application to subduction zone decarbonation, *Earth Planet. Sci. Lett.*, 236, 524–541, doi:10.1016/j.epsl.2005.04.033.
- Connolly, J. A. D. (2009), The geodynamic equation of state: What and how, *Geochim. Geophys. Geosyst.*, 10, Q10014, doi:10.1029/2009GC002540.
- Falloon, T. J., D. H. Green, L. V. Danyushevsky, and U. H. Faul (1999), Peridotite melting at 1.0 and 1.5 GPa: An experimental evaluation of techniques using diamond aggregates and mineral mixes for determination of near-solidus melts, *J. Petrol.*, 40, 1343–1375, doi:10.1093/ptroj/40.9.1343.
- Fram, M. S., C. E. Lesher, and A. M. Volpe (1998), Mantle melting systematics: Transition from continental to oceanic volcanism on the southeast Greenland margin, in *Proceedings of the Ocean Drilling Program, Scientific Results*, vol. 152, edited by A. D. Saunders, H. C. Larsen, and S. W. Wise, pp. 373–386, Ocean Drilling Program, College Station, Tex.
- Gast, P. W. (1968), Trace element fractionation and the origin of tholeiitic and alkaline magma types, *Geochim. Cosmochim. Acta*, 32, 1057–1086, doi:10.1016/0016-7037(68)90108-7.
- Gast, P. W., G. R. Tilton, and C. Hedge (1964), Isotopic composition of lead and strontium from Ascension and Gough Islands, *Science*, 145, 1181–1185, doi:10.1126/science.145.3637.1181.
- Ghiorso, M. S., M. M. Hirschmann, P. W. Reiners, and I. I. Kress, and C. Victor (2002), The pMELTS: A revision of MELTS for improved calculation of phase relations and major element partitioning related to partial melting of the mantle to 3 GPa, *Geochim. Geophys. Geosyst.*, 3(5), 1030, doi:10.1029/2001GC000217.
- Hauri, E. H. (1996), Major-element variability in the Hawaiian mantle plume, *Nature*, 382, 415–419, doi:10.1038/382415a0.
- Herzberg, C. T. (2011), Identification of source lithology in the Hawaiian and Canary Islands: Implications for origins, *J. Petrol.*, 52, 113–146, doi:10.1093/ptology/egg075.
- Herzberg, C. T., P. D. Asimow, N. T. Arndt, Y. Niu, C. M. Lesher, J. G. Fitton, M. J. Cheadle, and A. D. Saunders (2007), Temperatures in ambient mantle and plumes: Constraints from basalts, picrites, and komatiites, *Geochim. Geophys. Geosyst.*, 8, Q02006, doi:10.1029/2006GC001390.

- Herzberg, C. T., and M. J. O'Hara (2002), Plume-associated ultramafic magmas of Phanerozoic age, *J. Petrol.*, *43*, 1857–1883, doi:10.1093/ptetrology/43.10.1857.
- Hirschmann, M. M. (2000), Mantle solidus: Experimental constraints and the effects of peridotite composition, *Geochem. Geophys. Geosyst.*, *1*, 1042, doi:10.1029/2000GC000070.
- Hirschmann, M. M. (2006), Water, melting, and the deep Earth H<sub>2</sub>O cycle, *Annu. Rev. Earth Planet. Sci.*, *34*, 629–653, doi:10.1146/annurev.earth.34.031405.125211.
- Hirschmann, M. M., and E. M. Stolper (1996), A possible role for garnet pyroxenite in the origin of the “garnet signature” in MORB, *Contrib. Mineral. Petrol.*, *124*, 185–208, doi:10.1007/s004100050184.
- Hirschmann, M. M., P. D. Asimow, M. S. Ghiorso, and E. M. Stolper (1999), Calculation of peridotite partial melting from thermodynamic models of minerals and melts. III. Controls on isobaric melt production and the effect of water on melt production, *J. Petrol.*, *40*, 831–851, doi:10.1093/ptetroj/40.5.831.
- Hirschmann, M. M., T. Kogiso, M. B. Baker, and E. M. Stolper (2003), Alkalic magmas generated by partial melting of garnet pyroxenite, *Geology*, *31*, 481–484, doi:10.1130/0091-7613(2003).
- Hofmann, A. W., and W. M. White (1982), Mantle plumes from ancient oceanic crust, *Earth Planet. Sci. Lett.*, *57*, 421–436, doi:10.1016/0012-821X(82)90161-3.
- Horn, I., S. F. Foley, S. E. Jackson, and G. A. Jenner (1994), Experimentally determined partitioning of high field strength and selected transition elements between spinel and basaltic melt, *Chem. Geol.*, *117*, 193–218, doi:10.1016/0009-2541(94)90128-7.
- Huang, S., and F. A. Frey (2005), Recycled oceanic crust in the Hawaiian Plume: Evidence from temporal geochemical variations within the Koolau Shield, *Contrib. Mineral. Petrol.*, *149*, 556–575, doi:10.1007/s00410-005-0664-9.
- Itô, G., and J. J. Mahoney (2005), Flow and melting of a heterogeneous mantle: 1. Method and importance to the geochemistry of ocean island and mid-ocean ridge basalts, *Earth Planet. Sci. Lett.*, *230*, 29–46, doi:10.1016/j.epsl.2004.10.035.
- Itô, G., Y. Shen, G. Hirth, and C. J. Wolfe (1999), Mantle flow, melting, and dehydration of the Iceland mantle plume, *Earth Planet. Sci. Lett.*, *165*, 81–96, doi:10.1016/S0012-821X(98)00216-7.
- Iwamori, H., D. P. McKenzie, and E. Takahashi (1995), Melt generation by isentropic mantle upwelling, *Earth Planet. Sci. Lett.*, *134*, 253–266, doi:10.1016/0012-821X(95)00122-5.
- Johnson, K. T. M., H. J. B. Dick, and N. Shimizu (1990), Melting in the oceanic upper mantle: An ion microprobe study of diopsides in abyssal peridotites, *J. Geophys. Res.*, *95*, 2661–2678, doi:10.1029/JB095iB03p02661.
- Katz, R. F., and J. F. Rudge (2011), The energetics of melting fertile heterogeneities within the depleted mantle, *Geochem. Geophys. Geosyst.*, *12*, Q0AC16, doi:10.1029/2011GC003834.
- Katz, R. F., and S. M. Weatherley (2012), Consequences of mantle heterogeneity for melt extraction at mid-ocean ridges, *Earth Planet. Sci. Lett.*, *335–336*, 226–237, doi:10.1016/j.epsl.2012.04.042.
- Katz, R. F., M. Spiegelman, and C. H. Langmuir (2003), A new parameterization of hydrous mantle melting, *Geochem. Geophys. Geosyst.*, *4*(9), 1073, doi:10.1029/2002GC000433.
- Kelemen, P. B., G. Hirth, N. Shimizu, M. Spiegelman, and H. J. B. Dick (1997), A review of melt migration processes in the adiabatically upwelling mantle beneath oceanic spreading ridges, *Philos. Trans. R. Soc. London A*, *355*, 283–318, doi:10.1098/rsta.1997.0010.
- Kelemen, P. B., N. Shimizu, and V. J. M. Salters (1995), Extraction of mid-ocean-ridge basalt from the upwelling mantle by focused flow of melt in dunite channels, *Nature*, *375*, 747–753, doi:10.1038/375747a0.
- Kimura, J.-I., and H. Kawabata (2014), Trace element mass balance in hydrous adiabatic mantle melting: The Hydrous Adiabatic Mantle Melting Simulator version 1 (HAMMS1), *Geochem. Geophys. Geosyst.*, *15*, 2467–2493, doi:10.1002/2014GC005333.
- Kimura, J.-I., and H. Kawabata (2015), Ocean Basalt Simulator version 1 (OBS1): Trace element mass balance in adiabatic melting of a pyroxenite-bearing peridotite, *Geochem. Geophys. Geosyst.*, *16*, 267–300, doi:10.1002/2014GC005606.
- Kinzler, R. J., and T. L. Grove (1992a), Primary magmas of mid-ocean ridge basalts 1. Experiments and methods, *J. Geophys. Res.*, *97*, 6885–6906, doi:10.1029/91JB02840.
- Kinzler, R. J., and T. L. Grove (1992b), Primary magmas of mid-ocean ridge basalts 2. Applications, *J. Geophys. Res.*, *97*, 6907–6926, doi:10.1029/91JB02841.
- Klein, E. M. (2003), Geochemistry of the igneous oceanic crust, in *Treat. Geochem.*, *2*, 3433–463, doi:10.1016/B0-08-043751-6/03030-9.
- Klein, E. M., and C. H. Langmuir (1987), Global correlations of ocean ridge basalt chemistry with axial depth and crustal thickness, *J. Geophys. Res.*, *92*, 8089–8115, doi:10.1029/JB092iB08p08089.
- Klemme, S. (2004), The influence of Cr on the garnet–spinel transition in the Earth's mantle: Experiments in the system MgO–Cr<sub>2</sub>O<sub>3</sub>–SiO<sub>2</sub> and thermodynamic modelling, *Lithos*, *77*, 639–646, doi:10.1016/j.lithos.2004.03.017.
- Klemme, S., and H. S. C. O'Neill (2000), The near-solidus transition from garnet lherzolite to spinel lherzolite, *Contrib. Mineral. Petrol.*, *138*, 237–248, doi:10.1007/s004100050560.
- Klemme, S., J. D. Blundy, and B. J. Wood (2002), Experimental constraints on major and trace element partitioning during partial melting of eclogite, *Geochim. Cosmochim. Acta*, *66*, 3109–3123, doi:10.1016/S0016-7037(02)00859-1.
- Klemme, S., D. Günther, K. Hametner, S. Prowatke, and T. Zack (2006), The partitioning of trace elements between ilmenite, ulvöspinel, armalcolite and silicate melts with implications for the early differentiation of the moon, *Chem. Geol.*, *234*, 251–263, doi:10.1016/j.chemgeo.2006.05.005.
- Kogiso, T., and M. M. Hirschmann (2006), Partial melting experiments of bimineralic eclogite and the role of recycled mafic oceanic crust in the genesis of ocean island basalts, *Earth Planet. Sci. Lett.*, *249*, 188–199, doi:10.1016/j.epsl.2006.07.016.
- Kogiso, T., M. M. Hirschmann, and D. J. Frost (2003), High-pressure partial melting of garnet pyroxenite: Possible mafic lithologies in the source of ocean island basalts, *Earth Planet. Sci. Lett.*, *216*, 603–617, doi:10.1016/S0012-821X(03)00538-7.
- Kogiso, T., M. M. Hirschmann, and P. W. Reiners (2004), Length scales of mantle heterogeneities and their relationship to ocean island basalt geochemistry, *Geochim. Cosmochim. Acta*, *68*, 345–360, doi:10.1016/S0016-7037(03)00419-8.
- Koornneef, J. M., A. Stracke, B. Bourdon, M. A. Meier, K. P. Jochum, B. Stoll, and K. Grönvold (2012), Melting of a Two-component Source beneath Iceland, *J. Petrol.*, *53*, 127–157, doi:10.1093/ptetrology/egr059.
- Lambart, S., D. Laporte, A. Provost, and P. Schiano (2012), Fate of pyroxenite-derived melts in the peridotitic mantle: Thermodynamic and experimental constraints, *J. Petrol.*, *53*, 451–476, doi:10.1093/ptetrology/egr068.
- Lambart, S., D. Laporte, and P. Schiano (2013), Markers of the pyroxenite contribution in the major-element compositions of oceanic basalts: Review of the experimental constraints, *Lithos*, *160–161*, 14–36, doi:10.1016/j.lithos.2012.11.018.
- Langmuir, C. H., J. F. Bender, A. E. Bence, G. N. Hanson, and S. R. Taylor (1977), Petrogenesis of basalts from the FAMOUS area: Mid-Atlantic Ridge, *Earth Planet. Sci. Lett.*, *36*, 133–156, doi:10.1016/0012-821X(77)90194-7.

- Langmuir, C. H., E. M. Klein, and T. Plank (1992), Petrological systematics of mid-ocean ridge basalts: Constraints on melt generation beneath ocean ridges, in *Mantle Flow and Melt Generation at Mid-Ocean Ridges*, *Geophys. Monogr. Ser.*, vol. 71, edited by J. Phipps Morgan et al., pp. 183–280, AGU, Washington, D. C.
- Laporte, D., M. J. Toplis, M. Seyler, and J.-L. Devidal (2004), A new experimental technique for extracting liquids from peridotite at very low degrees of melting: Application to partial melting of depleted peridotite, *Contrib. Mineral. Petrol.*, *146*, 463–484, doi:10.1007/s00410-003-0509-3.
- Lee, C.-T. A., P. Luffi, T. Plank, H. Dalton, and W. P. Leeman (2009), Constraints on the depths and temperatures of basaltic magma generation on Earth and other terrestrial planets using new thermobarometers for mafic magmas, *Earth Planet. Sci. Lett.*, *279*, 20–33, doi:10.1016/j.epsl.2008.12.020.
- McKenzie, D. P. (1984), The generation and compaction of partially molten rock, *J. Petrol.*, *25*, 713–765, doi:10.1093/petrology/25.3.713.
- McKenzie, D. P. (1985), 230Th-238U disequilibrium and the melting processes beneath ridge axes, *Earth Planet. Sci. Lett.*, *72*, 149–157, doi:10.1016/0012-821X(85)90001-9.
- McKenzie, D. P., and M. J. Bickle (1988), The volume and composition of melt generated by extension of the lithosphere, *J. Petrol.*, *29*, 625–679, doi:10.1093/petrology/29.3.625.
- McKenzie, D. P., and R. K. O’Nions (1991), Partial melt distributions from inversion of rare earth element concentrations, *J. Petrol.*, *32*, 1021–1091, doi:10.1093/petrology/32.5.1021.
- McKenzie, D. P., and R. K. O’Nions (1995), The source regions of Ocean Island Basalts, *J. Petrol.*, *36*, 133–159, doi:10.1093/petrology/36.1.133.
- Nakagawa, T., P. J. Tackley, F. Deschamps, and J. A. D. Connolly (2012), Radial 1-D seismic structures in the deep mantle in mantle convection simulations with self-consistently calculated mineralogy, *Geochem. Geophys. Geosyst.*, *13*, Q11002, doi:10.1029/2012GC004325.
- Niu, Y., and R. Batiza (1991), An empirical method for calculating melt compositions produced beneath mid-ocean ridges: Application for axis and off-axis (seamounts) melting, *J. Geophys. Res.*, *96*, 21,753–21,777, doi:10.1029/91JB01933.
- Niu, Y., and M. J. O’Hara (2003), Origin of ocean island basalts: A new perspective from petrology, geochemistry, and mineral physics considerations, *J. Geophys. Res.*, *108*(B4), 2209, doi:10.1029/2002JB002048.
- O’Hara, M. J. (1968), The bearing of phase equilibria studies in synthetic and natural systems on the origin and evolution of basic and ultrabasic rocks, *Earth Sci. Rev.*, *4*, 69–133, doi:10.1016/0012-8252(68)90147-5.
- O’Neill, H. S. C. (1981), The transition between spinel lherzolite and garnet lherzolite, and its use as a geobarometer, *Contrib. Mineral. Petrol.*, *77*, 185–194, doi:10.1007/BF00636522.
- Pertermann, M., and M. M. Hirschmann (2003a), Partial melting experiments on a MORB-like pyroxenite between 2 and 3 GPa: Constraints on the presence of pyroxenite in basalt source regions from solidus location and melting rate, *J. Geophys. Res.*, *108*(B2), 2125, doi:10.1029/2000JB000118.
- Pertermann, M., and M. M. Hirschmann (2003b), Anhydrous partial melting experiments on MORB-like eclogite: Phase relations, phase compositions and mineral-melt partitioning of major elements at 2–3 GPa, *J. Petrol.*, *44*, 2173–2201, doi:10.1093/petrology/egg074.
- Pertermann, M., M. M. Hirschmann, K. Hametner, D. Günther, and M. W. Schmidt (2004), Experimental determination of trace element partitioning between garnet and silica-rich liquid during anhydrous partial melting of MORB-like eclogite, *Geochem. Geophys. Geosyst.*, *5*, Q05A01, doi:10.1029/2003GC000638.
- Phipps Morgan, J. (2001), Thermodynamics of pressure release melting of a veined plum pudding mantle, *Geochem. Geophys. Geosyst.*, *2*, 1001, doi:10.1029/2000GC000049.
- Pilet, S., M. B. Baker, O. Müntener, and E. M. Stolper (2011), Monte Carlo simulations of metasomatic enrichment in the lithosphere and implications for the source of alkaline basalts, *J. Petrol.*, *52*, 1415–1442, doi:10.1093/petrology/egr007.
- Plank, T., and C. H. Langmuir (1992), Effects of the melting regime on the composition of the oceanic crust, *J. Geophys. Res.*, *97*, 19,749–19,770, doi:10.1029/92JB01769.
- Plank, T., M. Spiegelman, C. H. Langmuir, and D. W. Forsyth (1995), The meaning of “mean F”: Clarifying the mean extent of melting at ocean ridges, *J. Geophys. Res.*, *100*, 15,045–15,015, doi:10.1029/95JB01148.
- Press, W., S. Teukolsky, and B. Flannery (1992), *Numerical Recipes in FORTRAN: The Art of Scientific Computing*, 2nd ed., Cambridge Univ. Press, N. Y.
- Putirka, K. D. (2016), Rates and styles of planetary cooling on Earth, Moon, Mars, and Vesta, using new models for oxygen fugacity, ferriferous ratios, olivine-liquid Fe-Mg exchange, and mantle potential temperature, *Am. Mineral.*, *101*, 819–840, doi:10.2138/am-2016-5402.
- Putirka, K. D., M. R. Perfit, F. J. Ryerson, and M. G. Jackson (2007), Ambient and excess mantle temperatures, olivine thermometry, and active vs. passive upwelling, *Chem. Geol.*, *241*, 177–206, doi:10.1016/j.chemgeo.2007.01.014.
- Robinson, J. A. C., and B. J. Wood (1998), The depth of the spinel to garnet transition at the peridotite solidus, *Earth Planet. Sci. Lett.*, *164*, 277–284, doi:10.1016/S0012-821X(98)00213-1.
- Robinson, J. A. C., B. J. Wood, and J. D. Blundy (1998), The beginning of melting of fertile and depleted peridotite at 1.5 GPa, *Earth Planet. Sci. Lett.*, *155*, 97–111, doi:10.1016/S0012-821X(97)00162-3.
- Rudge, J. F., J. MacLennan, and A. Stracke (2013), The geochemical consequences of mixing melts from a heterogeneous mantle, *Geochim. Cosmochim. Acta*, *114*, 112–143, doi:10.1016/j.gca.2013.03.042.
- Salters, V. J. M., and A. Stracke (2004), Composition of the depleted mantle, *Geochem. Geophys. Geosyst.*, *5*, Q05B07, doi:10.1029/2003GC000597.
- Schilling, J.-G. (1973), Iceland mantle plume: Geochemical study of Reykjanes Ridge, *Nature*, *242*, 565–571, doi:10.1038/242565a0.
- Schilling, J.-G., and J. W. Winchester (1969), Rare earth contributions to the origin of Hawaiian Lavas, *Contrib. Mineral. Petrol.*, *23*, 27–37, doi:10.1007/BF00371330.
- Shaw, D. M. (1970), Trace element fractionation during anatexis, *Geochim. Cosmochim. Acta*, *34*, 237–243, doi:10.1016/0016-7037(70)90009-8.
- Shen, Y., and D. W. Forsyth (1995), Geochemical constraints on initial and final depths of melting beneath ridges, *J. Geophys. Res.*, *100*, 2211–2237, doi:10.1029/94JB02768.
- Shorttle, O., J. MacLennan, and S. Lambart (2014), Quantifying lithological variability in the mantle, *Earth Planet. Sci. Lett.*, *395*, 24–40, doi:10.1016/j.epsl.2014.03.040.
- Sleep, N. H. (1984), Tapping of magmas from ubiquitous mantle heterogeneities: An alternative to mantle plumes?, *J. Geophys. Res.*, *89*, 10,029–10,041, doi:10.1029/JB089iB12p10029.
- Sleep, N. H. (1990), Hotspots and mantle plumes: Some phenomenology, *J. Geophys. Res.*, *95*, 6715–6736, doi:10.1029/JB095iB05p06715.
- Smith, P. M., and P. D. Asimow (2005), *Adiabat\_1ph*: A new public front-end to the MELTS, pMELTS, and pHMELTS models, *Geochem. Geophys. Geosyst.*, *6*, Q02004, doi:10.1029/2004GC000816.
- Sobolev, A. V., A. W. Hofmann, S. V. Sobolev, and I. K. Nikogosian (2005), An olivine-free mantle source of Hawaiian shield basalts, *Nature*, *434*, 590–597, doi:10.1038/nature03411.

- Sotin, C., and E. M. Parmentier (1989), Dynamical consequences of compositional and thermal density stratification beneath spreading centers, *Geophys. Res. Lett.*, *16*, 835–838, doi:10.1029/GL016i008p00835.
- Spiegelman, M., and D. P. McKenzie (1987), Simple 2-D models for melt extraction at mid-ocean ridges and island arcs, *Earth Planet. Sci. Lett.*, *83*, 137–152, doi:10.1016/0012-821X(87)90057-4.
- Stixrude, L., and C. Lithgow-Bertelloni (2011), Thermodynamics of mantle minerals - II. Phase equilibria, *Geophys. J. Int.*, *184*, 1180–1213, doi:10.1111/j.1365-246X.2010.04890.x.
- Stolper, E. M., and P. D. Asimow (2007), Insights into mantle melting from graphical analysis of one-component systems, *Am. J. Sci.* *307*, 1051–1139, doi:10.2475/08.2007.01.
- Stracke, A. (2012), Earth's heterogeneous mantle: A product of convection-driven interaction between crust and mantle, *Chem. Geol.*, *330–331*, 274–299, doi:10.1016/j.chemgeo.2012.08.007.
- Stracke, A., and B. Bourdon (2009), The importance of melt extraction for tracing mantle heterogeneity, *Geochim. Cosmochim. Acta*, *73*, 218–238, doi:10.1016/j.gca.2008.10.015.
- Stracke, A., B. Bourdon, and D. P. McKenzie (2006), Melt extraction in the Earth's mantle: Constraints from U–Th–Pa–Ra studies in oceanic basalts, *Earth Planet. Sci. Lett.*, *244*, 97–112, doi:10.1016/j.epsl.2006.01.057.
- Stracke, A., A. Zindler, V. J. M. Salters, D. P. McKenzie, J. Blichert-Toft, F. Albarede, and K. Gronvold (2003a), Theistareykir revisited, *Geochem. Geophys. Geosyst.*, *4*(2), 8507, doi:10.1029/2001GC000201.
- Stracke, A., A. Zindler, V. J. M. Salters, D. P. McKenzie, and K. Gronvold (2003b), The dynamics of melting beneath Theistareykir, northern Iceland, *Geochem. Geophys. Geosyst.*, *4*(10), 8513, doi:10.1029/2002GC000347.
- Sun, C., and Y. Liang (2013), The importance of crystal chemistry on REE partitioning between mantle minerals (garnet, clinopyroxene, orthopyroxene, and olivine) and basaltic melts, *Chem. Geol.*, *358*, 23–36, doi:10.1016/j.chemgeo.2013.08.045.
- Sun, C., and Y. Liang (2014), An assessment of subsolidus re-equilibration on REE distribution among mantle minerals olivine, orthopyroxene, clinopyroxene, and garnet in peridotites, *Chem. Geol.*, *372*, 80–91, doi:10.1016/j.chemgeo.2014.02.014.
- Sun, S. S., and W. F. McDonough (1989), Chemical and isotopic systematics of oceanic basalts: Implications for mantle composition and processes, *Geol. Soc. Spec. Publ.*, *42*, 313–345, doi:10.1144/GSL.SP.1989.042.01.19.
- Till, C. B., L. T. Elkins-Tanton, and K. M. Fischer (2010), A mechanism for low-extent melts at the lithosphere-asthenosphere boundary, *Geochem. Geophys. Geosyst.*, *11*, Q10015, doi:10.1029/2010GC003234.
- Turcotte, D. L., and J. L. Ahern (1978), A porous flow model for magma migration in the asthenosphere, *J. Geophys. Res.*, *83*, 767–772, doi:10.1029/JB083iB02p00767.
- Walter, M. J. (1998), Melting of garnet peridotite and the origin of komatiite and depleted lithosphere, *J. Petrol.* *39*, 29–60, doi:10.1093/ptro/39.1.29.
- Walter, M. J., T. Katsura, A. Kubo, T. Shinmei, O. Nishikawa, E. Ito, C. E. Lesher, and K. Funakoshi (2002), Spinel-garnet lherzolite transition in the system CaO-MgO-Al<sub>2</sub>O<sub>3</sub>-SiO<sub>2</sub> revisited: An in situ X-ray study, *Geochim. Cosmochim. Acta*, *66*, 2109–2121, doi:10.1016/S0016-7037(02)00845-1.
- Wasylenki, L. E., M. B. Baker, A. J. R. Kent, and E. M. Stolper (2003), Near-solidus melting of the shallow upper mantle: Partial melting experiments on depleted peridotite, *J. Petrol.*, *44*, 1163–1191, doi:10.1093/ptrology/44.7.1163.
- White, R. S., D. P. McKenzie, and R. K. O'Nions (1992), Oceanic crustal thickness from seismic measurements and rare earth element inversions, *J. Geophys. Res.*, *97*, 19,683–19,715, doi:10.1029/92JB01749.
- Wood, D. A. (1979), Dynamic partial melting: Its application to the petrogeneses of basalts erupted in Iceland, the Faeroe Islands, the Isle of Skye (Scotland) and the Troodos Massif (Cyprus), *Geochim. Cosmochim. Acta*, *43*, 1031–1046, doi:10.1016/0016-7037(79)90092-9.
- Wood, B. J., and J. D. Blundy (2003), Trace element partitioning under crustal and uppermost mantle conditions: The influences of ionic radius, cation charge, pressure, and temperature, *Treat. Geochem.*, *2*, 395–424.
- Workman, R. K., and S. R. Hart (2005), Major and trace element composition of the depleted MORB mantle (DMM), *Earth Planet. Sci. Lett.*, *231*, 53–72, doi:10.1029/2003GC000568.
- Zindler, A., S. R. Hart, F. A. Frey, and S. P. Jakobsson (1979), Nd and Sr isotope ratios and rare earth element abundances in Reykjanes Peninsula basalts evidence for mantle heterogeneity beneath Iceland, *Earth Planet. Sci. Lett.*, *45*, 249–262, doi:10.1016/0012-821X(79)90127-4.